Gondwana Research 112 (2022) 1–23

Contents lists available at ScienceDirect

Gondwana Research

journal homepage: www.elsevier.com/locate/gr

Does tectonic deformation control episodic continental arc magmatism? Evidence from granitic magnetic fabrics (AMS)

A. Burton-Johnson [a,*], T.R. Riley [a], R.J. Harrison [b], C. Mac Niocaill [c], J.R. Muraszko [b,d], P.D. Rowley [e]

[a] British Antarctic Survey, High Cross, Madingley Road, Cambridge CB3 0ET, UK
[b] Department of Earth Sciences, University of Cambridge, Cambridge CB2 3EQ, UK
[c] Department of Earth Sciences, University of Oxford, Oxford OX1 3AN, UK
[d] School of Earth and Space Sciences, Peking University, Haidian District, Dachengfang, Beijing, China
[e] Geological Mapping Inc., New Harmony, UT 84757, USA

ARTICLE INFO

Article history:
Received 9 June 2021
Revised 18 August 2022
Accepted 15 September 2022
Available online 21 September 2022
Handling Editor: Taras Gerya

Keywords:
Tectonic-magmatic relations
Continental arcs
Flare-up events
Granitic intrusions
Anisotropy of magnetic susceptibility
Antarctica

ABSTRACT

This paper applies magnetic fabric analyses to plutons of the East Pacific continental arc. Continental arc magmatism is strongly episodic, with voluminous granitic magma addition occurring during discrete high-flux events ('flare-ups'). The cause of these flare-ups is debated, variously invoking tectonic, mantle, or crustal controls. To understand how the syn-magmatic strain history changes during a flare-up, we compare granitic magnetic fabric (Anisotropy of Magnetic Susceptibility, AMS) and geochronological data from the Antarctic Peninsula (Lassiter Coast), Sierra Nevada, and Chile. This comparison indicates a common pattern in orientation and magnitude of syn-magmatic deformation, showing flare-up events occur during increased tectonic compression driven by enhanced interplate coupling and fast subduction. Flare-ups terminate as tectonic compression reduces or the regime becomes extensional, even if convergence rates remain high. As with enhanced seismicity, magmatic flare-ups result from high tectonic compression, during discrete periods of enhanced interplate coupling within broader periods of increased subduction rates. The enhanced magmatic flux results either from crustal thickening leading to partial melting of a newly accreted, hydrous mafic underplate, enhanced melt segregation in the source, or in response to high tectonic compression rendering lithostatic compression the weakest compressive force, enhancing magma extraction and ascent from the mantle.

© 2022 The Authors. Published by Elsevier B.V. on behalf of International Association for Gondwana Research. This is an open access article under the CC BY license (http://creativecommons.org/licenses/by/4.0/).

1. Introduction

1.1. Magmatic flare-up events

The evolution of the continental crust is intrinsically linked to the emplacement of granitic material via continental arc magmatism, imparting the comparative low density that prevents continent destruction at subduction zones. Continental arc magmatism is episodic, occurring in 10–30 My long "flare-ups" between 20 and 70 My intervals (DeCelles et al., 2009), with 1–4 My magmatic episodicity at individual magmatic centres during each flare-up (De Silva et al., 2015). Whether these flare-ups convert into net crustal growth depends on the relative proportions of mantle-derived and crustal sources, and the volume of new material compared with that lost through erosion, basal crust delamination, and forearc subduction erosion (de Silva and Kay, 2018).

Periods of high magmatic flux (termed "flare-up events") have been attributed to crustal, mantle, magmatic, and tectonic processes. The circum-Pacific mid-Cretaceous flare-up was attributed to plate reorganisation and consequent deformation (Matthews et al., 2012), invoking tectonic modification of the rates and obliquity of subduction. However, Ducea (2001) compared the apparent intrusive flux for the Sierra Nevada with the rate or obliquity of subduction and found no correlation. Instead, intra-crustal processes were proposed, with either under-thrusting or crustal thickening and lithospheric delamination driving crustal melting (DeCelles et al., 2009; Ducea, 2001). Crustal thickening was invoked to explain the apparent shared episodicity between tectonic deformation and magmatism of the Sierra Nevada (Cao et al., 2015), based on visible mineral fabrics, host rock structures, and sedimentary units. However, radiogenic isotopes indicate a dominantly mantle, not crustal source for the East Pacific

* Corresponding author.
E-mail address: alerto@bas.ac.uk (A. Burton-Johnson).

https://doi.org/10.1016/j.gr.2022.09.006
1342-937X/© 2022 The Authors. Published by Elsevier B.V. on behalf of International Association for Gondwana Research.
This is an open access article under the CC BY license (http://creativecommons.org/licenses/by/4.0/).

flare-ups (Ardila et al., 2019). Tectono-magmatic processes and the overriding plate may contribute over different timescales; tectonics, crustal thickening and delamination controlling first order periods of high magmatic activity (40–60 My) whilst magmatic processes (melt, segregation, ascent) and upper-crustal tectonics control higher frequency events (20 to < 1 My) (de Saint Blanquat et al., 2011; De Silva et al., 2015).

With all these competing hypotheses and observations, it remains unclear how or if magmatic flare-up events are affected by *syn*-magmatic tectonic deformation. This paper investigates this relationship by applying an alternative approach, collecting and collating magnetic mineral fabric data of plutons from along the East Pacific continental arc. By determining the degree of *syn*-magmatic deformation from this data, and comparing this degree with the geochronology and apparent magmatic flux of the plutons analysed, we can test how the changing *syn*-magmatic deformation regime affects magmatic episodicity.

1.2. Anisotropy of magnetic susceptibility (AMS)

To compare tectonic deformation and flare-up events, the first challenge is determining whether the two are coincident. Although U-Pb dating provides accurate geochronology, and global plate models (e.g. Seton et al., 2012) constrain convergence rates, determining the nature and scale of *syn*-magmatic deformation is difficult. This is because 'traditional' structural evidence (faults and dykes) record the *post*-magmatic deformation of their host pluton, as they fracture or intrude the pluton after its crystallisation.

Instead, the pluton's magnetic mineral fabric (AMS) is a potential record of *syn*-magmatic deformation. AMS data describes the foliation and lineation of a sample's magnetic mineral fabric via three orthogonal axes (Fig. 1): the maximum susceptibility axis (K1) defines the magnetic lineation; the minimum susceptibility axis (K3) is the pole to the magnetic foliation; and the intermediate axis (K2) is the orthogonal intermediate axis within the magnetic foliation plane.

The AMS fabric reflects the anisotropic distribution and orientation of magnetic minerals in a sample. As with other mineral fabrics, AMS axes relate to the *syn*-magmatic strain present during the final stages of crystallisation (Paterson et al., 1998). This strain generates the magnetic lineation (K1) in its maximum extension direction (e_1), and the magnetic foliation perpendicular to the maximum shortening direction (e_3) (Fig. 1).

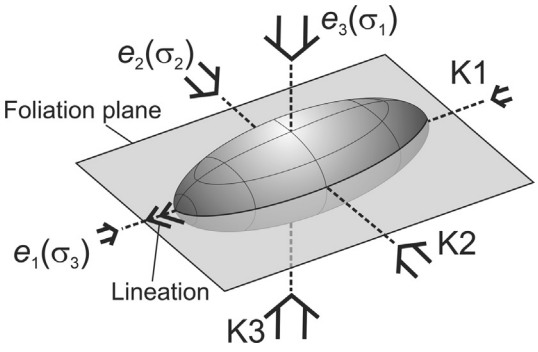

Fig. 1. Relationship of magnetic mineral fabrics (foliation and lineation) and the principal vectors of magnetic susceptibility describing the AMS fabric (K1 – Maximum susceptibility; K2 – Intermediate susceptibility; K3 – Minimum susceptibility) to the strain ellipsoid and strain axes (e_1 – Maximum extension direction; e_2 – Intermediate extension direction; e_3 – Minimum extension direction). To illustrate how these axes relate to crystallisation under coaxial pure shear, in parentheses are the principal stress directions that would generate these axes during coaxial *syn*-magmatic deformation (σ_1 – Maximum compression direction; σ_2 – Intermediate compression direction; σ_3 – Minimum compression direction). Adapted from Burton-Johnson et al. (2019). Arrow sizes reflect relative stress intensity under pure shear.

The *syn*-magmatic strain producing AMS fabrics has variably been proposed to originate from tectonic deformation or magmatic emplacement processes, or a combination of the two. Burton-Johnson et al. (2019) compared anisotropy of magnetic susceptibility (AMS) axes with tectonic deformation axes for various worldwide plutons in both compressional and extensional regimes. They proposed that when more than ~ 100 m from internal or external contacts, whole-pluton AMS fabrics in compressional and extensional regimes dominantly record coaxial tectonic deformation fabrics rather than magmatic emplacement processes (Fig. 2, with data sources in Table 1). From the 100 km^2 Mt Kinabalu pluton (Borneo; Burton-Johnson et al., 2019) to the 1,100 km^2 Tuolumne Batholith (California; Titus et al., 2005), contact-parallel magmatic fabrics are generally not observed even < 100 m from the margins. However, on a local scale within a pluton there is abundant evidence for emplacement and non-coaxial deformation fabrics. In addition to internal and external contact-parallel foliations (e.g. the Mt Kinabalu pluton, Burton-Johnson et al., 2019), this includes fabric rotation during *syn*-magmatic shearing (e.g. the sigmoidal fabric of the Mono Creek pluton [de Saint Blanquat and Tikoff, 1997], and *syn*-magmatic shearing of the Cathedral Peak Granite by the Cascade Shear Zone [Tikoff et al., 2005]); fabric rotation during emplacement of subsequent units (e.g. vertical inflation of the Papoose Flat pluton [de Saint-Blanquat et al., 2001], and lateral rotation of the Joshua Flat pluton [Morgan et al., 2013]); or mechanical interactions during crystallisation (Olivier et al., 1997). Pluton-scale and local-scale tectonic and magmatic fabrics are thus both invaluable for our understanding of intrusive magmatic processes.

When AMS fabrics record tectonic strain, the strain axes (the maximum extension direction, e_1, the intermediate, e_2, and the minimum, e_3; Fig. 1) relate to the *syn*-magmatic tectonic stress axes (the maximum compression direction, σ_1, the intermediate, σ_2, and the minimum, σ_3; Fig. 1 illustrates this relationship for pure shear). These axes orient according to the relative magnitudes of the two principle sources of differential stress within the lithosphere (Burton-Johnson et al., 2019): 1) Subvertical lithostatic compression; and 2) subhorizontal tectonic compression. During high tectonic compression (Fig. 3a), subhorizontal tectonic compression is the dominant stress (σ_1) and the subvertical lithostatic compression is the weakest stress (σ_3). Consequently, under coaxial pure shear, the foliation pole (e_3 and K3) is subhorizontal (parallel to σ_1), whilst the lineation direction (e_1 and K1; parallel to σ_3) is subvertical. During extension (Fig. 3d), subvertical lithostatic compression is σ_1 and the direction of crustal extension is σ_3. Here, K1 (e_1) is subhorizontal in the direction of extension, and K3 (e_3) is subvertical.

Between high tectonic compression and extension are two intermediate pure shear regimes (Fig. 3b and 3c). If subhorizontal tectonic compression is σ_1, but subvertical lithostatic compression is the intermediate (σ_2) rather than weakest stress, then both K1 and K3 are subhorizontal (Fig. 3b). This reflects moderate tectonic compression. If tectonic compression is lower still, then lithostatic compression becomes σ_1, K3 becomes subvertical, and σ_3 and K1 become subhorizontal and orthogonal to the tectonic compression direction (Fig. 3c).

Finally, where AMS records simple, non-coaxial shear, the maximum extension direction (e_1, K1) rotates towards the plane of shear, and the shortening direction (e_3, K3) rotates towards perpendicular to the shear plane (Fig. 3e). Where a pluton emplaces along an active shear zone, the fabrics adjacent to the shear zone will record non-coaxial shear rather than the coaxial shear recorded across the rest of the pluton. However, even the Cascade Lake Shear Zone on the eastern margin of the Tuolumne Batholith

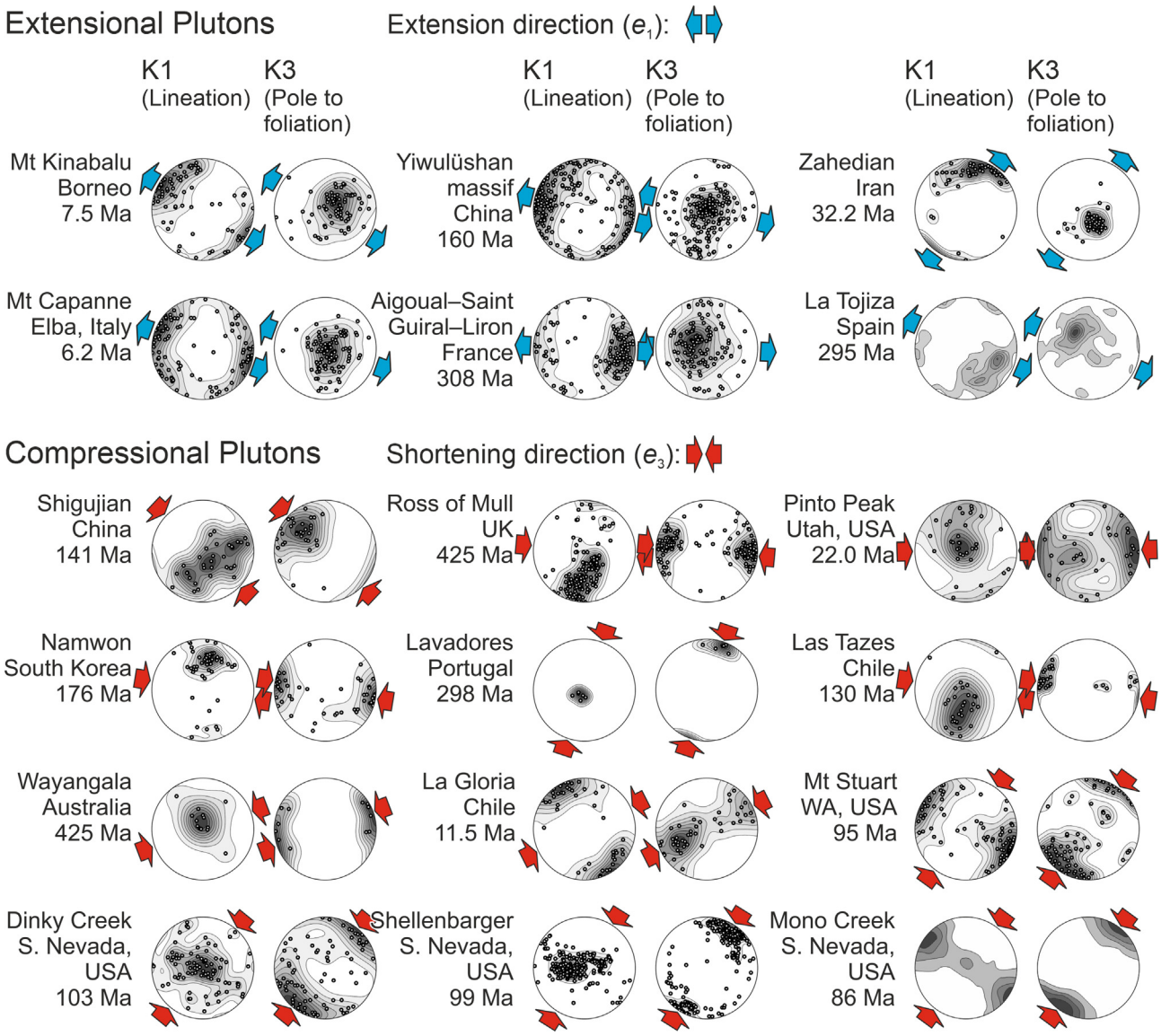

Fig. 2. Global compilation of lineation (K1, e_1) and pole to foliation (K3, e_3) directions of AMS data from intrusions emplaced in both extensional and compressive tectonic settings showing the orientation of the principal extensional or shortening direction generating the tectonic fabric (adapted from Burton-Johnson et al., 2019). Note that (despite their wide range of ages and scales) in all plutons emplaced in an extensional setting the foliation is subhorizontal and the lineation is subparallel to the *syn*-magmatic crustal extension direction. Conversely, in all plutons emplaced in a compressional setting, the foliation is subvertical and strikes perpendicular to the *syn*-magmatic compression direction. These common relationships between the AMS fabric and the *syn*-magmatic deformation regime indicate that AMS fabrics dominantly record coaxial tectonic deformation rather than magmatic emplacement processes. AMS and geochronology data sources, number of samples analysed, and dating method used are shown in Table 1.

only generated non-coaxial deformation fabrics up to 1 km from the shear zone, despite the extended cooling history of the batholith compared to smaller plutons (Tikoff et al., 2005).

Note that whilst the direction of lithostatic compression is always subvertical, the direction of subhorizontal tectonic shortening (e_3) is not always parallel with the plate convergence direction. During pure convergence, the angle between the plate margin and the convergent plate motion vector (α) coincides with the angle (θ_P) between the plate margin and the tectonic shortening directions (i.e. $\alpha = \theta_P = 90°$). However, strain "refraction" occurs during oblique convergence resulting in the following linear relationship (Teyssier et al., 1995):

$$\theta_P = 0.5 * \left(90^{\circ} + \alpha\right) \quad (1)$$

For example, when $\alpha = 70°$, $\theta_P = 80°$. The result is that during oblique subduction, the tectonically-driven, horizontal shortening direction (e_3) is closer to perpendicular with the plate margin than the relative convergence directions would imply.

The above discussion assumes that the magnetic carrier phase from which the AMS fabric is derived is either multidomain magnetite, or paramagnetic phases whose preferred orientation generates a normal magnetic fabric (e.g. phyllosilicates such as biotite or chlorite, as well as amphiboles and pyroxenes; Hrouda, 1982). Although these are the dominant carrier phases in previous studies of plutonic AMS fabrics (see Table 1 and Table 2), where the magnetic fabric is hosted by single domain magnetite, this AMS fabric will be inverted and thus not represent the mineral axes (Rochette et al., 1992). However, the presence of single domain magnetite

Table 1
AMS and geochronology data sources, number of samples analysed, dominant magnetic carrier phase, and dating method used in the data compilation of Fig. 2.

Extensional Plutons (Fig. 2)					
Pluton	AMS			Geochronology	
	Source	# samples (# cores)	Dominant carrier phase	Source	Method
Mt Kinabalu	Burton-Johnson et al. (2019)	94	Magnetite (multidomain)	(Cottam et al., 2010)	U/Pb (zircon)
Yiwulüshan massif	(Lin et al., 2013a)	51 (302)	Variable (Magnetite and paramagnetic phases)	(Lin et al., 2013b)	U/Pb (zircon)
Zahedian	Sadeghian et al. (2005)	189	Magnetite (multidomain)	(Camp and Griffis, 1982)	K/Ar (biotite)
Mt Capanne	Bouillin et al. (1993)	74	Biotite (paramagnetic)	(Juteau et al., 1984)	U/Pb (zircon)
Aigoual – Saint Guiral– Liron	Talbot et al. (2005)	125	Biotite (paramagnetic)	(Monié et al., 2000)	Ar/Ar (biotite)
La Tojiza	Aranguren et al. (2003)	74 (296)	Biotite (paramagnetic)	(Fernández-Suárez et al., 2000)	U/Pb (zircon)
Compressional Plutons (Fig. 2)					
Pluton	AMS			Geochronology	
	Source	# samples (# cores)	Carrier phase	Source	Method
Shigujian	Deng et al. (2013)	33 (259)	Variable (Magnetite and paramagnetic phases)	Deng et al. (2013)	U/Pb (zircon)
Ross of Mull	Petronis et al. (2012)	139	Magnetite (multidomain)	(McAteer, 2009)	U/Pb (zircon)
Pinto Peak	Petronis and O'Driscoll (2013)	35 (789)	Magnetite (multidomain)	(Rowley, 1998)	Ar/Ar
Namwon	Otoh et al. (1999)	13	Variable (Magnetite and paramagnetic phases)	(Turek and Kim, 1995)	U/Pb (zircon)
Lavadores	Martins et al. (2011)	63	Magnetite	Martins et al. (2011)	U/Pb (zircon)
Las Tazas	Wilson (1998)	30 (133)	Magnetite	Wilson et al. (2000)	Ar/Ar (hornblende)
Wayangala	Lennox et al. (2016)	8	Biotite (paramagnetic)	(Lennox et al., 2014)	U/Pb (zircon)
La Gloria	Gutierrez et al. (2013)	46	Low-Ti magnetite (multidomain)	Deckart et al. (2010)	U/Pb (zircon)
Mt Stuart	(Benn et al., 2001)	75	Biotite, hornblende, and pyrrhotite (paramagnetic)	(Matzel et al., 2006)	U/Pb (zircon)
Dinky Creek	Cruden (1999)	83 (461)	Mixed multidomain magnetite and paramagnetic phases	Tobisch et al. (1993)	U/Pb (zircon)
Shellenbarger	Tomek et al. (2017)	240	Low-Ti magnetite (multidomain)	Lowe (1996)Fiske and Tobisch (1978)	U/Pb (single & multigrain zircon)Rb-Sr (WR)
Mono Creek	de Saint Blanquat and Tikoff (1997)	183 (1040)	Magnetite (multidomain)	Stern et al. (1981)	U/Pb (zircon)

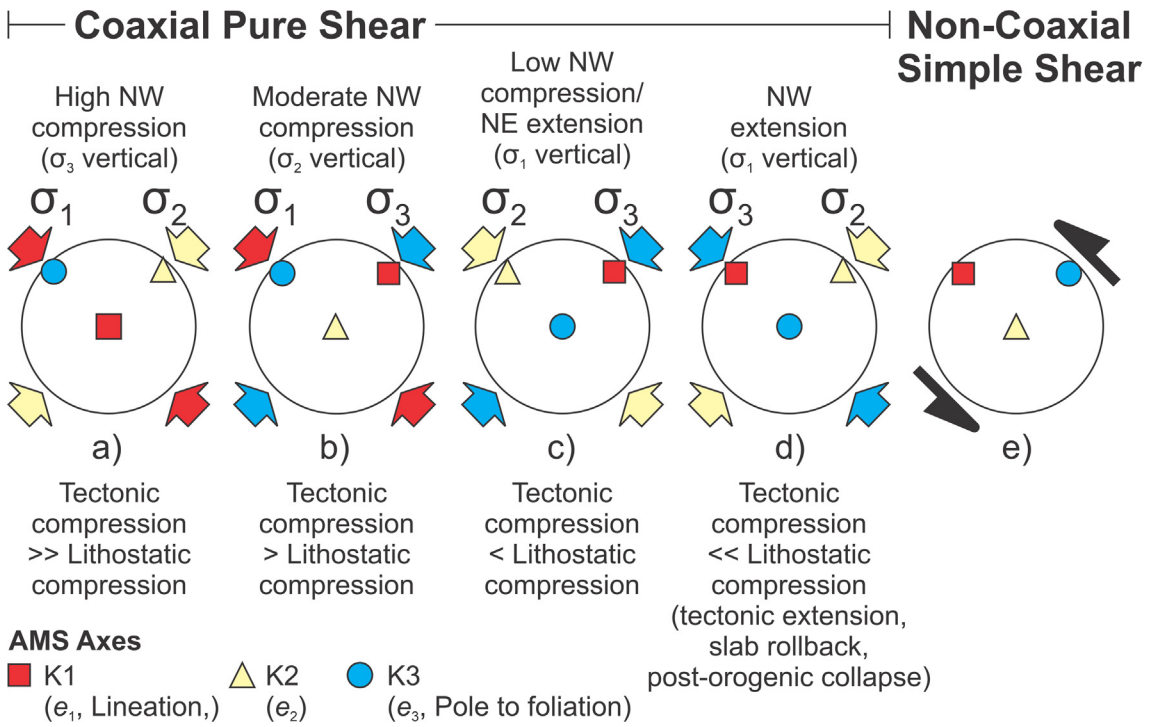

Fig. 3. Lower hemisphere stereonets for deriving the variable magnetic fabric orientations of the Lassiter Coast Intrusive Suite (Fig. 9) within a regime of homogenous vertical lithostatic compression and NW-SE oriented horizontal tectonic compression of consistent orientation but variable magnitude; resulting from the NW-SE subduction convergence direction of the Aluk Plate beneath the Antarctic Peninsula. Shown are the principal compressive stress directions (maximum stress, σ_1; intermediate stress, σ_2; and minimum stress, σ_3), simple shear directions, and vectors of magnetic susceptibility: K1 – Maximum susceptibility and magnetic lineation; K2 – Intermediate susceptibility; K3 – Minimum susceptibility and pole to foliation.

can be identified by thermomagnetic analyses, as well as hysteresis and first-order reversals curves (analysing the coercivity of the carrier phases). Similarly, some paramagnetic phases (tourmaline, cordierite, siderite, and goethite; Rochette et al., 1992) can also generate an inverse AMS fabric if they dominate the magnetic signature. Care must thus be taken with paramagnetic samples to petrographically identify the phases present.

2. The Lassiter Coast Intrusive Suite (LCIS)

Our previous work (Burton-Johnson et al., 2019) indicated a global ubiquity of tectonic fabrics in plutonic AMS data, albeit with a data compilation of 18 plutons. To test this observation, and investigate the relationship between AMS fabrics, magmatic addition rates, and changing tectonic regimes, we have tested our hypothesis using a Cretaceous magmatic flare up event: the Lassiter Coast Intrusive Suite (LCIS) of the Antarctic Peninsula.

The LCIS was one of the largest Mesozoic magmatic events of the Antarctic Peninsula (Burton-Johnson and Riley, 2015), and is composed of ~ 13,000 km^2 of pyroxenite to granite intrusions (Vaughan et al., 2012b), emplaced within an up to 6 km thick slate sequence of Jurassic mudstones to fine grained sandstones (the Latady Group). This sedimentary sequence was deposited in a back-arc basin setting (Riley et al., 2020) during the intraplate rifting of Gondwana (Willan, 2003). Previous U-Pb zircon data shows the LCIS was emplaced in three pulses: 130–126 Ma, 118–113 Ma, and 108–102 Ma (Riley et al., 2018).

We examined 26 separate plutons (Fig. 4), covering ~ 1,200 km^2. This subset ranges from composite batholiths to individual stocks, and covers the lithological range of the LCIS (pyroxenite to granite). In targeting plutons for sampling, we selected plutons across the length and breadth of the study area, whilst also representing the complete range of lithologies found in previous mapping (Rowley et al., 1992; Rowley and Williams, 1982). Geological units were mapped linking outcrops of similar mineralogy, including dividing plutons and batholiths into composite units of different mineral compositions and textures. It was notable (as elsewhere) that the more erosion-resistant plutonic outcrops made them preferentially exposed compared to the less competent sedimentary units, helping delineate the subice extent of the plutons (Fig. 4a). The aeromagnetic anomaly (Fig. 4b) was useful in this regard, but shows the geological effect on magnetic susceptibility at depth as well as on the bedrock surface (hence the different distribution of the magnetic anomaly, Fig. 4b, with the interpreted bedrock surface geology map, Fig. 4a).

Based on 500-stop modal point counting on K-feldspar-stained thin sections, most of the intrusions are classified as granodiorite (following Streckeisen, 1976), of which fine-medium grained biotite hornblende granodiorite is the most abundant lithology.

Slate formation requires > 1.6 kbar, equivalent to > 6 km depth (Bucher and Grapes, 2011). The common occurrence of andalusite in Latady Group slates < 600–800 m from intrusions indicates a < 3kbar shallow upper crustal emplacement pressure (Bucher and Grapes, 2011), equivalent to < 11 km depth (assuming a 2.8gcm^{-3} density for the Latady Group slates), and heating of the slates to > 350 °C. Cordierite occurrences < 200 m from the Mount Axworthy intrusion indicate contact metamorphic conditions of < 9 km (<2.5kbar) and > 500 °C (Bucher and Grapes, 2011). Based on these P-T constraints, we interpret emplacement of the entire LCIS at similar upper crustal depths.

3. Methodology

For U-Pb analysis, zircon crystals were separated from < 500 μm sieved fractions of powdered samples by panning; then hand-picked; mounted in epoxy; and polished. Their internal structure

Table 2
AMS and geochronology data sources, number of samples analysed, and dating method used in the AMS data compilation of the Sierra Nevada (USA) and Chile (Fig. 11). Approximate areas of the Sierra Nevada plutons calculated in GIS (used for the apparent intrusive flux calculations of Fig. 14).

Sierra Nevada Plutons						
Pluton	AMS			Geochronology		Approximate area (km^2)
	Source	# samples (# cores)	Dominant carrier phase	Source	Method	
a) Cathedral Peak	Titus et al. (2005)	14 (85)	Magnetite (multidomain) (Tikoff et al., 2005)	Coleman and Glazner (1997)	U/Pb (zircon)	582
b) Johnson Gt Pph	Titus et al. (2005)	49 (741)	Magnetite (multidomain)	Coleman and Glazner (1997)	U/Pb (zircon)	17
c) Jackass Lakes	McNulty et al. (1996)	40	Ferrimagnetic (magnetite?)	Stern et al. (1981)	U/Pb (zircon)	246
d) Mono Creek	de Saint Blanquat and Tikoff (1997)	183 (1040)	Magnetite (multidomain)	Stern et al. (1981)	U/Pb (zircon)	616
e) Round Valley Peak	Tikoff et al. (1999)	57	Magnetite	Stern et al. (1981)	U/Pb (zircon)	265
f) Silver Pass Pph	Titus et al. (2005)	17 (101)	Magnetite (multidomain) (de Saint Blanquat and Tikoff, 1997)	Titus et al. (2005)	Field relations	5
g) Shellenbarger	Tomek et al. (2017)	240	Low-Ti magnetite (multidomain)	Lowe (1996)Fiske and Tobisch (1978)	U/Pb (single & multigrain zircon)Rb-Sr (WR)	13
h) Dinkey Creek	Cruden (1999)	83 (461)	Mixed multidomain magnetite and paramagnetic phases	Tobisch et al. (1993)	U/Pb (zircon)	743
i) Bald Mountain	Tobisch and Cruden (1995)	18	Magnetite (multidomain)	Tobisch and Cruden (1995)	U/Pb (zircon)	65
j) Mt Barcroft	Michlesen (2004)	78 (655)	Mixed magnetite and paramagnetic phases	Ernst et al. (2003)	U/Pb (zircon)	100
k) Beer Creek	Morgan et al. (2013)	141	Magnetite (multidomain)	Gillespie Jr (1979) Coleman et al. (2003)	U/Pb (zircon)U/Pb (zircon)	273
l) Eureka Valley	Morgan et al. (2013)	17	Magnetite (multidomain)	Sylvester et al. (1978)	U/Pb (zircon)	17
m) Joshua Flat	Morgan et al. (2013)	153	Magnetite (multidomain)	Matty et al. (2008)	U/Pb (zircon)	158
n) Santa Rita Flat	Vines and Law (2000)	64 (461)	Magnetite	Chen (1977)	U/Pb (zircon)	137
o) Papoose Flat	de Saint-Blanquat et al. (2001)	102	Magnetite (multidomain)	Miller (1996)	U/Pb (monazite)	130

Chilean Plutons					
Pluton	AMS			Geochronology	
	Source	# samples (# cores)	Carrier phase	Source	Method
p) Fortuna	Somoza et al. (2015)	42	Magnetite (multidomain)	Campbell et al. (2006)Dilles et al. (1997)	U/Pb (zircon) U/Pb (zircon)
q) Los Picos	Somoza et al. (2015)	42	Magnetite (multidomain)	Campbell et al. (2006)Tomlinson et al. (2010)	U/Pb (zircon)U/Pb (zircon)
r) Las Tazas	Wilson (1998)	30 (133)	Magnetite	Wilson et al. (2000)	Ar/Ar (hornblende)
s) Illapel	Ferrando et al. (2014)	56 (492)	Magnetite (multidomain)	Ferrando et al. (2014)	Ar/Ar (biotite)
t) Concón	Creixell et al. (2006)	6 (49)	Magnetite	Hervé et al. (1988)	Rb/Sr (whole rock)
u) La Gloria	Gutierrez et al. (2013)	46	Low-Ti magnetite (multidomain)	Deckart et al. (2010)	U/Pb (zircon)
v) Huemel	Garibaldi et al. (2018)	40 (251)	Magnetite (multidomain)	Schaen et al. (2017)	U/Pb (zircon)

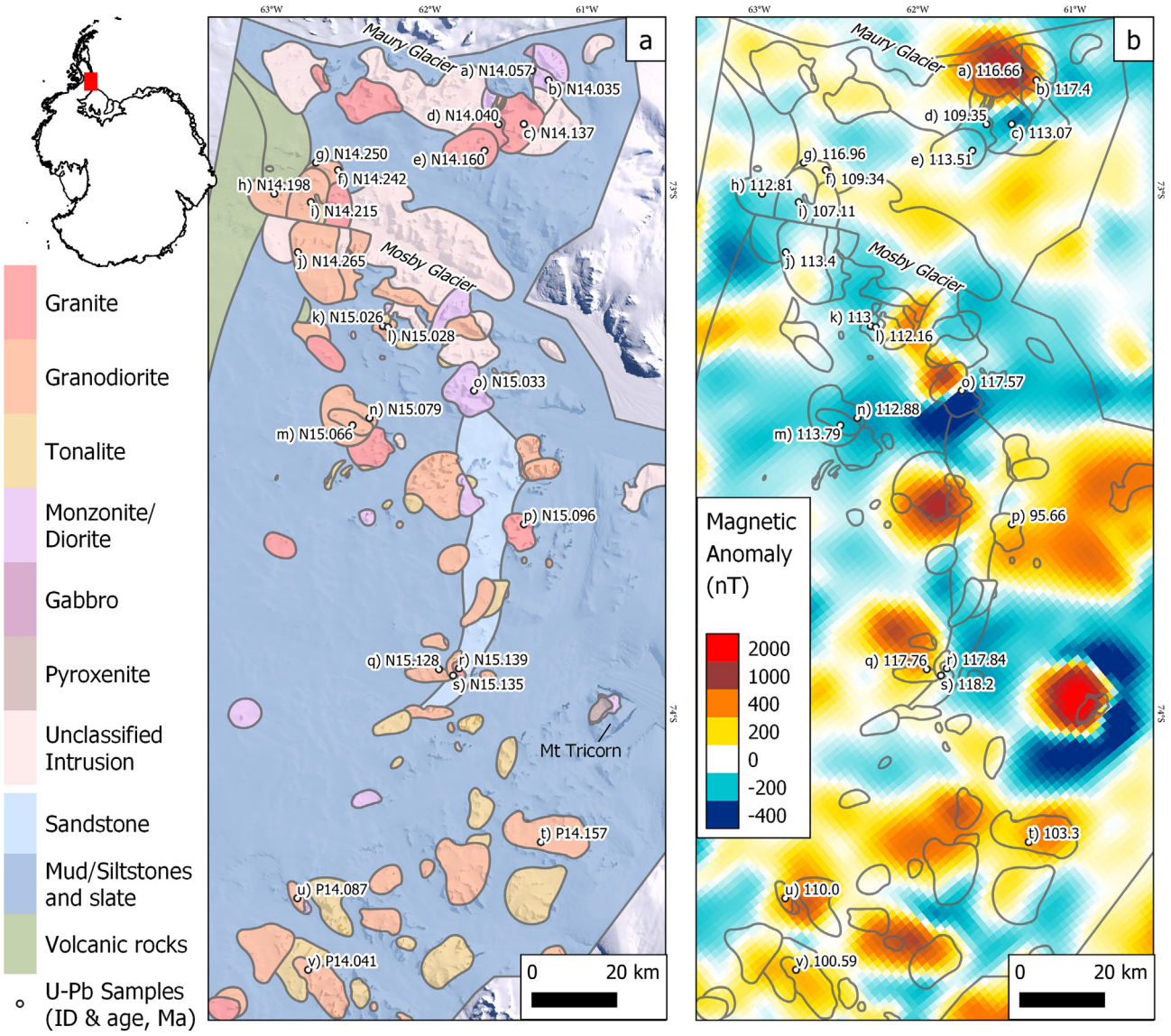

Fig. 4. a) Geological map of the study area with sample locations. b) Reduced to pole, magnetic anomaly data for the study area (Golynsky et al., 2018) overlain with outlines of the geological units and U-Pb zircon ages (this study).

was imaged by cathodoluminescence at the University of Edinburgh. U-Pb isotopic analysis was performed on a Cameca ims-1270 ion microprobe at the University of Edinburgh following the procedures of Kelly et al. (2008). Results were calibrated against zircon Geostandard 91500, which has a $^{206}Pb/^{238}U$ ratio of 0.17918 ± 8, a $^{206}Pb/^{238}U$ age of 1062.5 ± 0.4 Ma and U and Pb concentrations of 81.2 and 14.8 ppm (Wiedenbeck et al., 1995). In situ common Pb corrections were applied using the present day common Pb composition. $^{206}Pb/^{238}U$ concordia ages were calculated using Isoplot v3.7 (Ludwig, 2003). Uncertainty in the calculated pluton ages are presented as 95% confidence limits.

To determine the magnetic mineralogy, variability of magnetic susceptibility with temperature was analysed on powdered samples. An AGICO MFK1 Kappabridge with a CS4 high temperature attachment and CS-L low temperature attachment was used under an argon atmosphere to reduce secondary oxidation. A representative subset of the samples were selected for further magnetic characterisation of hysteresis and first-order reversal curves (FORC) using a Lakeshore Vibrating Sample Magnetometer.

263 oriented block samples were collected from the LCIS, from which 11 cm^3 cylindrical oriented cores were drilled at the University of Oxford. All magnetic susceptibility analyses were performed at the University of Cambridge. 1,425 oriented cores were analysed on an AGICO MFK1 Kappabridge to determine the orientation and magnitude (K) of the three principal axes of the AMS fabric (axis of maximum magnetic susceptibility, K1; intermediate susceptibility, K2; and minimum susceptibility, K3; Fig. 1). Each sub-specimen's results were normalised by the specimen's mean susceptibility (K_{mean}) and averaged for each block sample to determine mean values of the AMS ellipsoid (Jelínek and Kropáček, 1978; Owens, 2000).

4. Results

4.1. U-Pb zircon

All of the 22 samples analysed yielded mid-Cretaceous ages (118.2 ± 0.8 to 95.7 ± 0.7 Ma); comparable to previous studies of the LCIS (Pankhurst and Rowley, 1991; Riley et al., 2018; Vaughan et al., 2002a, 2002b). Given the number of samples and individual U-Pb analyses (369), full isotopic data and U-Th-Pb con-

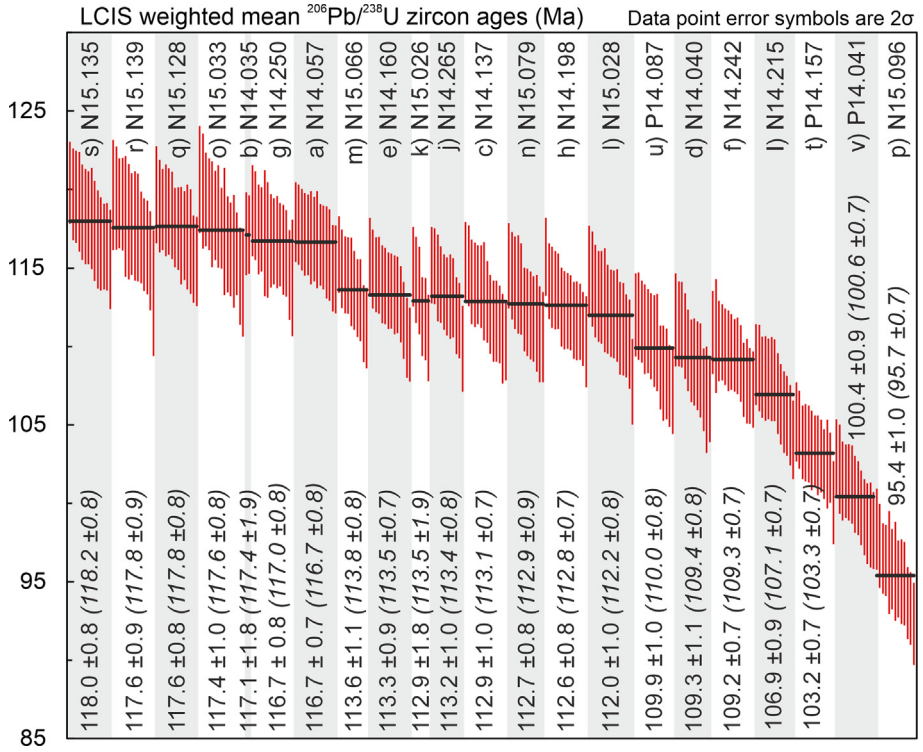

Fig. 5. Individual zircon $^{206}Pb/^{238}U$ ages (2σ error bars) and sample weighted mean ages for the LCIS. Calculated ages presented with 95% confidence limits. Concordia ages in parentheses, also with 95% confidence limits. Concordia plots and zircon cathodoluminescence images presented in the Supplementary Material. Sample names and pluton ID letters as in Fig. 4.

centrations, and representative cathodoluminescence zircon images are presented in the Supplementary Material. The ages and their spatial distribution are presented in Fig. 4b, their $^{206}Pb/^{238}U$ weighted mean ages in Fig. 5, and their $^{238}U/^{206}Pb$ concordia in the Supplementary Material. Of the 22 samples analysed, only 7 samples yielded evidence of inherited ages. These 23 inherited ages range from 118.7 ± 1.3 to 1483.2 ± 15.3 Ma and are excluded from the age calculations. Thirteen discordant ages of 100.7 ± 1.1 to 119.1 ± 1.8 Ma were also excluded as they were interpreted to be affected by Pb loss and potential radiation damage in high U grains (Supplementary Material). Given the zircon zoning of most samples (Supplementary Material), where the excluded ages are only slightly older than the concordant ages of their pluton, at least some these are likely to be from antecrysts or earlier crystal growth. The diorite N14.035 only yielded one zircon crystal, from which a concordant age was derived from two spots (Fig. 5 and Supplementary Material). Although 18 analyses were acquired from the 113.0 ± 1.1 Ma tonalite N15.026, 10 of these yielded inherited ages (132.7 ± 1.5 to 846.2 ± 9.9 Ma) and 2 ages were discordant (109.3 ± 1.2 and 115.7 ± 1.3 Ma), leaving only 6 concordant ages. Otherwise, all pluton ages were derived from 10 to 15 concordant analyses.

4.2. Magnetic mineralogy

The LCIS exhibit a range of magnetic susceptibilities (Fig. 6 and Fig. 7), with a higher susceptibility cluster representing ferromagnetic carrier phases, and a lower susceptibility cluster representing paramagnetic carrier phases (Fig. 7). Plotting the degree of magnetic anisotropy (P; $\frac{K1}{K3}$) against the mean bulk susceptibility (K_{mean}) divides the samples into two groups (Fig. 7a): a low susceptibility group of samples with a low degree of anisotropy (the paramagnetic samples), and a high susceptibility group with a high degree of anisotropy (the ferromagnetic samples). This shows that changes in mineralogy affect the degree of anisotropy in the LCIS.

All but the lowest susceptibility samples show abrupt reductions in bulk susceptibility on heating between 565 and 585 °C (the Curie temperature of pure magnetite; Fig. 6). Although a minor Hopkinson peak is identified prior to the 565–585 °C magnetic susceptibility reduction in some samples (Fig. 6b), the lack of an extreme peak indicates dominance of multidomain rather than single or pseudo single-domain particles (Orlický, 1990). FORC diagrams (Fig. 8) are sensitive indicators of single domain magnetite as even small proportions of single-domain grains produce a high coercivity and narrow bias range (Fig. 8; Harrison et al., 2018). However, none of the LCIS samples analysed display this behaviour. Consequently, the AMS data does not represent an inverse fabric (as would be produced by single-domain magnetite; Rochette et al., 1992; Stephenson et al., 1986).

The five lowest susceptibility plutons (Fig. 6b) lack the magnetite Curie temperature and the −148 °C susceptibility increase (the Verwey transition; Walz 2002), and thus have a paramagnetic carrier phase. As these five plutons are all biotite tonalites, biotite is the probable carrier. K3 is perpendicular to the cleavage plane in biotite (Martín-Hernández and Hirt, 2003), enabling direct comparison of the ferromagnetic and paramagnetic pluton fabrics.

Although the thermomagnetic and FORC data indicate multidomain magnetite is the dominant magnetic phase in the ferromagnetic plutons, for AMS studies it is important to identify whether the bulk magnetic phase also carries the magnetic anisotropy. This is because in rocks where the bulk magnetic phase is isotropic, less magnetically susceptible phases can control the magnetic anisotropy (Biedermann and Bilardello, 2021). Combining high and low field AMS data can separate the paramagnetic and ferromagnetic fabrics. However, the magnetic anisotropy of the rock's magnetocrystalline minerals cannot exceed the magnetic anisotropy of a single crystal. Therefore, if none of the "matrix" minerals in a

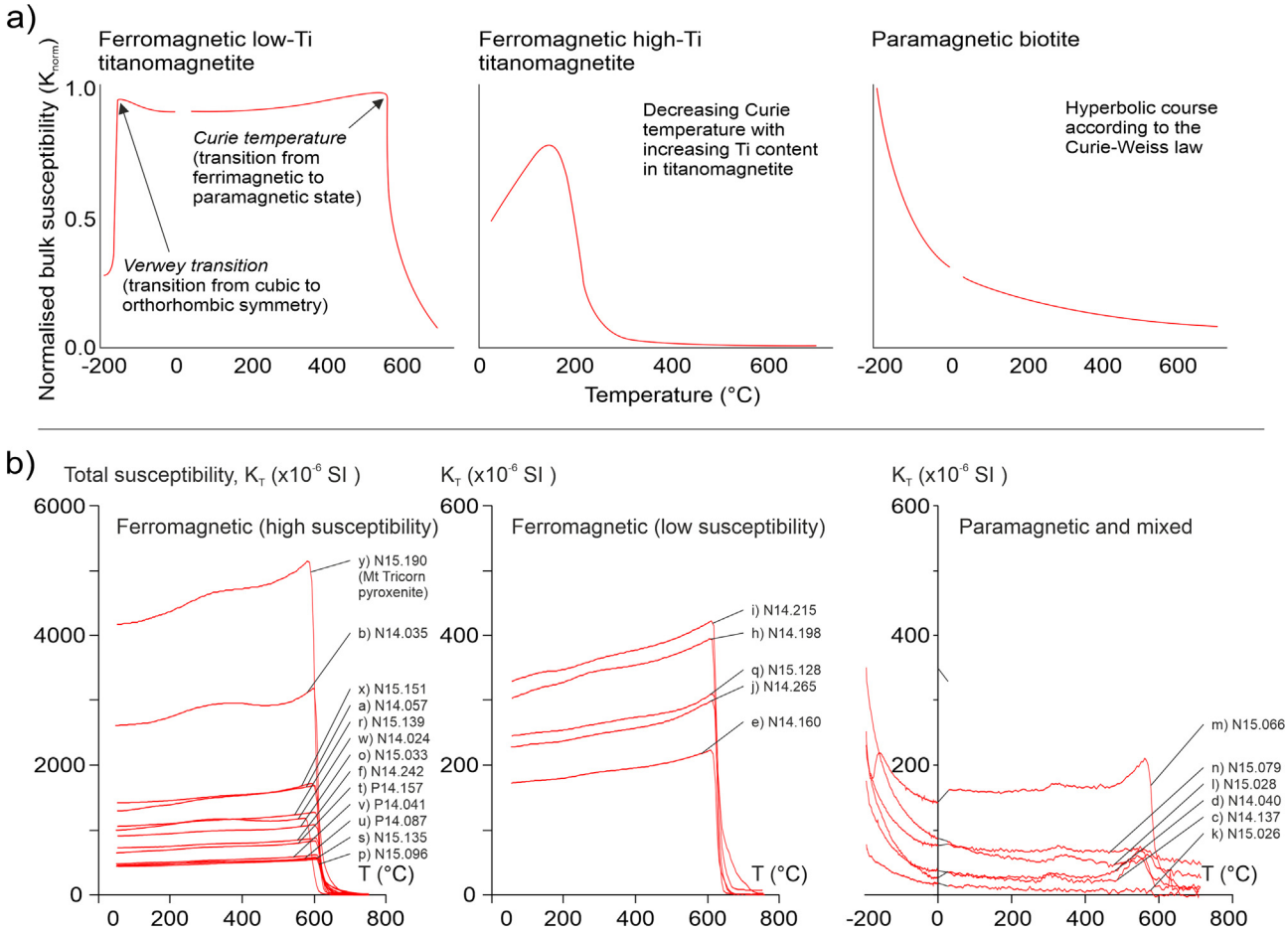

Fig. 6. a) Idealised variation of magnetic susceptibility with increasing temperature for ferromagnetic and paramagnetic carrier phases (adapted from Žák et al., 2021). b) Variation of magnetic susceptibility with increasing temperature for representative samples of each LCIS pluton. Pluton ID letters from Fig. 4 and Fig. 9.

sample possess large enough single-crystal values of mean bulk susceptibility (K_{mean}) and mean deviatoric susceptibility (K', Equation (2)) compared with the sample values, then it is likely that magnetite is the dominant carrier of magnetic anisotropy (Biedermann and Bilardello, 2021). For the LCIS, this comparison (Fig. 7c) shows the deviatoric susceptibility (K') for all the paramagnetic plutons to be below the single crystal value of biotite, supporting our prior conclusion that biotite is the carrier phase for the AMS fabric. For all but one ferromagnetic pluton, K' exceeds the single crystal values of the magnetocrystalline "matrix" minerals, indicating that magnetite (determined above to be multidomain) is the dominant carrier phase of magnetic anisotropy in the LCIS.

$$K' = \sqrt{\frac{(K_1 - K_{mean})^2 + (K_2 - K_{mean})^2 + (K_3 - K_{mean})^2}{3}} \quad (2)$$

The lowest susceptibility ferromagnetic pluton (pluton 'm. N15.066' in Fig. 6b) displays a mixed signature, with a paramagnetic hyperbolic variation in susceptibility below 0 °C, and the abrupt drop in susceptibility at 565–585 °C associated with magnetite. It's K' value exceeds that for hornblende or phlogopite, but is below that for biotite. We conclude that its AMS fabric is carried by a combination of multidomain magnetite and biotite, but as K3 is perpendicular to the cleavage plane in biotite, the fabrics of these two phases are comparable.

One pluton appears to have a spuriously high susceptibility value of 0.32 K_{mean}. However, this pluton is the exceptionally magnetite-rich Mt Tricorn pyroxenite cumulate (pluton 'y' in the SE of Fig. 9). This body (a pyroxenite mountain, 11 km across and 1.5 km high) represents the highest susceptibility aeromagnetic anomaly on the Antarctic Peninsula (Golynsky et al., 2018).

4.3. AMS fabrics

Full AMS data are presented in the Supplementary Material along with maps of the full foliation and lineation data. All the plutons analysed display a dominant AMS fabric, albeit with varying degrees of data dispersion (Fig. 9). To ensure the statistical significance of the individual analyses, we applied the test for triaxial anisotropy of Jelínek (1977). By excluding samples from pluton-scale analyses where $F_{2,9} < 8.0215$, we ensure that all samples used are triaxially anisotropic at the 99 % significance level. Even with this high significance level, only 4 of the 1,425 oriented cores analysed were excluded. When collated, the pluton-scale foliation poles (K3) show a dominant fabric across the LCIS with a steep WNW foliation dip (206/21 NW, Fig. 10a). However, this foliation has a variable dip across the suite (Fig. 10a). The lineation of the AMS fabrics (K1) is dominantly shallowly plunging to the NNE but varies from steeply plunging to shallowly plunging in a NNE-SSW direction (Fig. 10b).

5. Differentiating tectonic and magmatic strain in the AMS data

Whether the LCIS AMS data dominantly records magmatic rather than tectonic strain can be tested by comparing the AMS and mineral fabric data with field evidence for tectonic strain

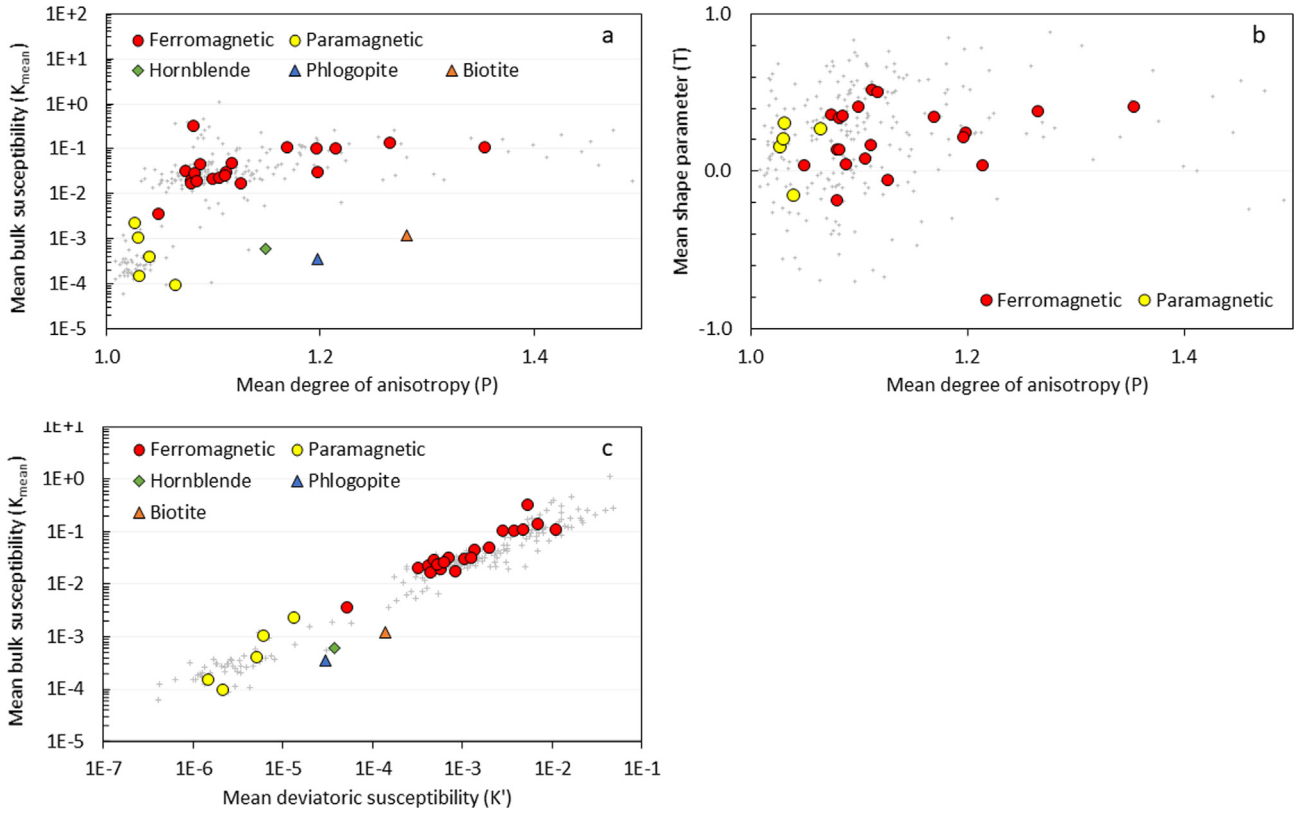

Fig. 7. Scalar AMS parameters of all LCIS site analyses (small grey crosses) and overall parameters of each pluton, classified as either ferromagnetic or paramagnetic based on their thermomagnetic profiles (Fig. 6). Single crystal properties of hornblende, biotite, and phlogopite are shown for comparison (Biedermann et al., 2020, 2018, 2014) and included in the Supplementary Material. Bulk susceptibility values are volume normalised (no unit, SI).

(Paterson et al., 1998). Except when porphyritic, the LCIS lack visible fabrics However, that the AMS fabric is representative of the mineral fabrics of the LCIS is supported by the foliation of mafic enclaves measured in the field (Fig. 10c, average foliation of 201°/77° NW). However, the AMS fabric is more homogenous than the enclave fabric; this homogeneity of plutonic AMS fabrics having been highlighted elsewhere (Bouchez, 1997; Olivier et al., 1997). "Homogenous" in this case meaning that the overall AMS fabric (Fig. 10a and Fig. 10b) has axes clustered unimodally about mean values (Olivier et al., 1997), and can be defined by the orthogonal axes of a single strain ellipse (e_1, e_2, and e_3; Fig. 1), rather than displaying a multimodal or random distribution. Similarly, each individual pluton AMS fabric can also be described as "homogenous" (Fig. 9) despite the variability between plutons.

As AMS foliation poles orient parallel to the principal shortening direction (Fig. 1), if the overall LCIS AMS fabric (Fig. 10a and Fig. 10b) is tectonically derived then this indicates a *syn*-emplacement WNW-ESE oriented tectonic shortening. The Latady Group country rocks were subjected to the pre-, syn-, and post-magmatic deformation history of the LCIS. The bedding orientations dip predominantly steeply towards the WNW (196°/62° NW, Fig. 10d), very similar to the AMS and enclave foliation; again indicating reorientation and tilting about a WNW-ESE directed shortening direction. The mafic dykes crosscutting the LCIS postdate the intrusions, and consistently display subvertical WNW-ESE striking orientations (293°/90°, Fig. 10e). Because dykes strike in the direction of maximum lateral compression (excluding local pre-existing crustal weaknesses; Sielfeld et al., 2017), this indicates that the strain regime remained WNW-ESE compressional after emplacement of their host pluton.

The close agreement between the AMS and field data indicates that the AMS fabric records tectonic, not magmatic strain, and that this strain was consistently WNW-ESE shortening pre-, syn-, and post-emplacement. Paleomagnetic data from the LCIS indicates that the WNW-ESE recorded orientation of this shortening direction has undergone minimal rotation since LCIS emplacement (5.3°±22.9° ACW, or 0.8°±28.9° CW; Kellogg and Reynolds, 1978). Assuming 0° rotation, the shortening direction indicated by the average AMS foliation (116°), average enclave foliation (111°), tilted sedimentary beds (106°), and dykes (113°) compares with the 114° Late Cretaceous (83–68 Ma) subduction azimuth of the Aluk Plate beneath the Antarctic Peninsula at this latitude (McCarron and Larter, 1998), indicating coaxial subduction-driven deformation for all structures (note that the lack of a complete plate circuit prior to 83 Ma prevents deduction of older convergence directions by kinematic modelling).

6. Origin of the AMS fabric variation

All the AMS data of the LCIS dominantly record *syn*-magmatic tectonic deformation. The fabrics dominantly record WNW-ESE oriented *syn*-magmatic crustal shortening, sub-parallel to the *syn*-magmatic plate convergence direction between the subducting Aluk Plate and the overriding Antarctic Plate. However, the relative orientations of the AMS fabric's orthogonal axes (K1, K2, and K3) are variable (Fig. 9). Multiple samples were collected across each pluton to compensate for variation from local magmatic fabrics (similar to those observed in pluton macro fabrics; e.g. Paterson et al., 2019) and contact-parallel strain (Tikoff et al., 2005). Although these magmatic sources of variability will contribute to the data distribution of each sample, the overall AMS axes of most plutons remain coaxial with the regional strain axes and the overall fabric (Fig. 10), even if their relative orientations vary. This vari-

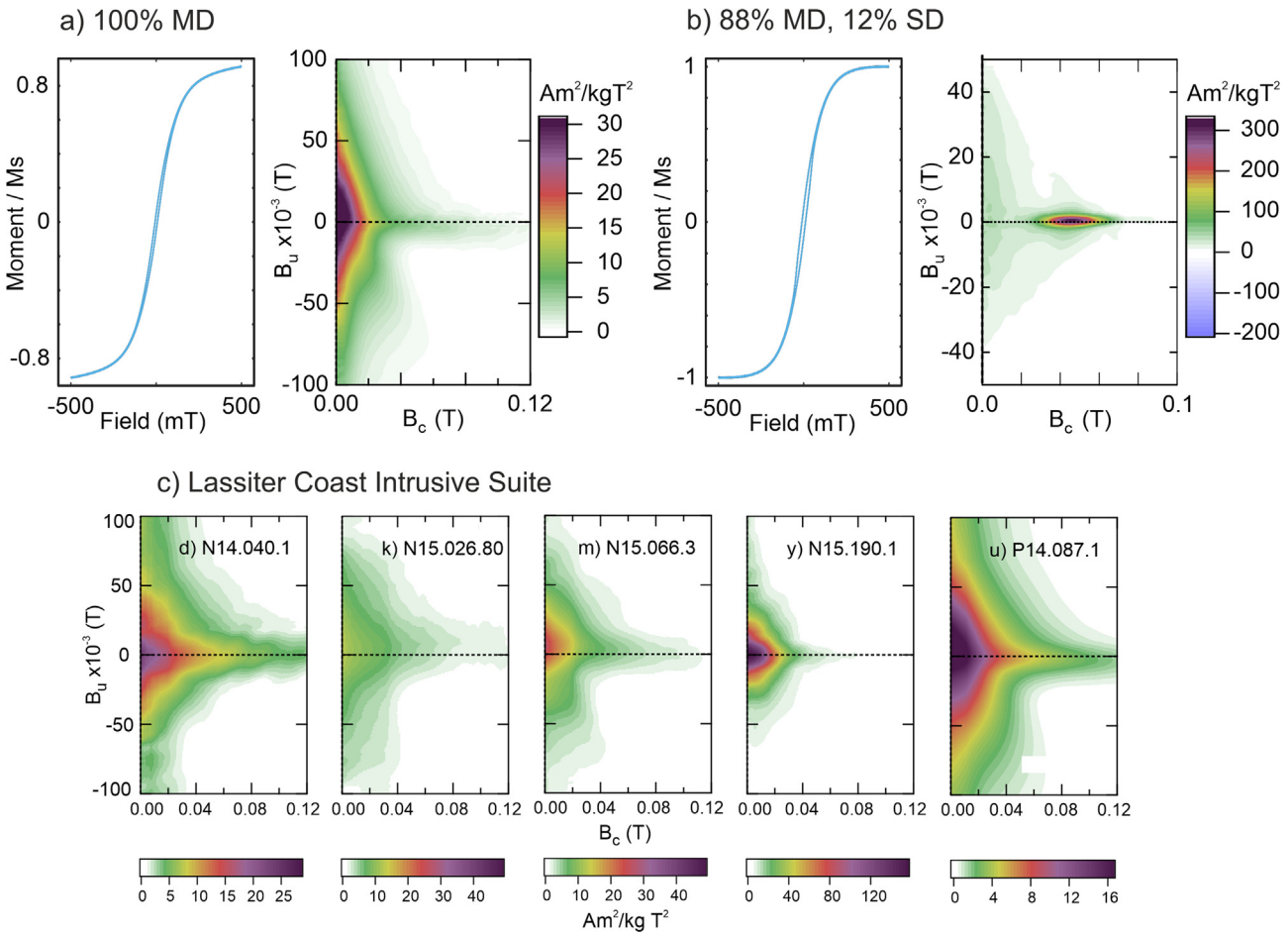

Fig. 8. Hysteresis loops and First Order Reversal Curves (FORC diagrams) for two synthetic binary mixtures of a) purely multi-domain (MD), and b) a mixture of multi- and single-domain (SD) magnetite, showing the sensitivity and response of FORC diagrams in determining the presence of SD grains even when the proportion in undetectable on hysteresis loops (Harrison et al., 2018). c) FORC diagrams for the Lassiter Coast Intrusive Suite, showing an absence of SD behaviour. Pluton ID letters from Fig. 4 and Fig. 9.

ability was highlighted in the previous compilation of selected global data (Burton-Johnson et al., 2019). Consequently, the dominant control on this variability are the relative magnitudes of tectonic and lithostatic compression, and the resultant orientations of the strain axes. We can thus interpret the variable AMS fabrics of Fig. 9 following the classification of Fig. 3. The classification of each pluton's fabric within this conceptual model of pure and simple shear is shown by the stereonet outlines in Fig. 9. Some fabrics are straightforward to classify, as two poles lie in a subhorizontal plane and one in a subvertical orientation (e.g. Plutons "i" and "g" in Fig. 9). However, the poles of other plutons are oblique to these orientations (e.g. Plutons "d" and "o"). In these cases, the pole closest to vertical is used, and the others treated as subhorizontal for classification. However, as shown by the overall fabric above, most plutons display one subvertical and two subhorizontal poles.

For most of the LCIS, the pole to the foliation (K3) is variable within a WNW-ESE striking plane (Fig. 10a), whilst the lineation direction (K1) is variable within a NNE-SSW striking plane (Fig. 10b), indicating high to low degree WNW-ESE coaxial tectonic compression and shortening (Fig. 3a-c). There are four examples where K3 is steeply plunging and K1 plunges shallowly NW-SE (orthogonal to its NNE-SSW dominant plane). This represents convergence-parallel extension (Fig. 3d), driven by extensional tectonics (e.g. slab rollback) or post-orogenic collapse.

One example shows a shallowly NNE dipping K3 and WNW dipping K1. Because K3 represents the maximum shortening direction (e_3), and K1 the minimum shortening direction (e_1), this variability could indicate multiple deformation regimes (as proposed by Vaughan et al., 2012a). However, there is no evidence for secondary folding of the sedimentary beds (Fig. 10), nor is there evidence for this in the relative regional plate motions (Matthews et al., 2016). Instead, the orientation can be explained through local non-coaxial simple shear (Fig. 3e; Arbaret et al., 1997; Benn, 2010), rather than the coaxial pure shear recorded by the other plutons of the LCIS.

7. East Pacific AMS fabrics

Both our previous data compilation (Burton-Johnson et al., 2019) and the new AMS data from the LCIS indicate that AMS data at a pluton-scale dominantly records *syn*-magmatic tectonic deformation. To test how ubiquitous this is, we have compiled all published AMS data and associated geochronology on two well-studied regions: Chile and the Sierra Nevada (California, Fig. 11). Unlike Tierra del Fuego, Central America, and Alaska, these regions have not undergone large-scale block rotation. We summarise the data contributing to this compilation below and in Table 2. Note from Table 2 that multidomain magnetite is the most prevalent carrier phase in the East Pacific plutons, removing complications of single-domain inverted fabrics in the ferromagnetic plutons (Orlický, 1990). Where the fabric is paramagnetic, biotite is the dominant carrier phase, for which K3 is perpendicular to the cleavage plane (Martín-Hernández and Hirt, 2003). Consequently, the ferromagnetic and paramagnetic pluton fabrics are comparable.

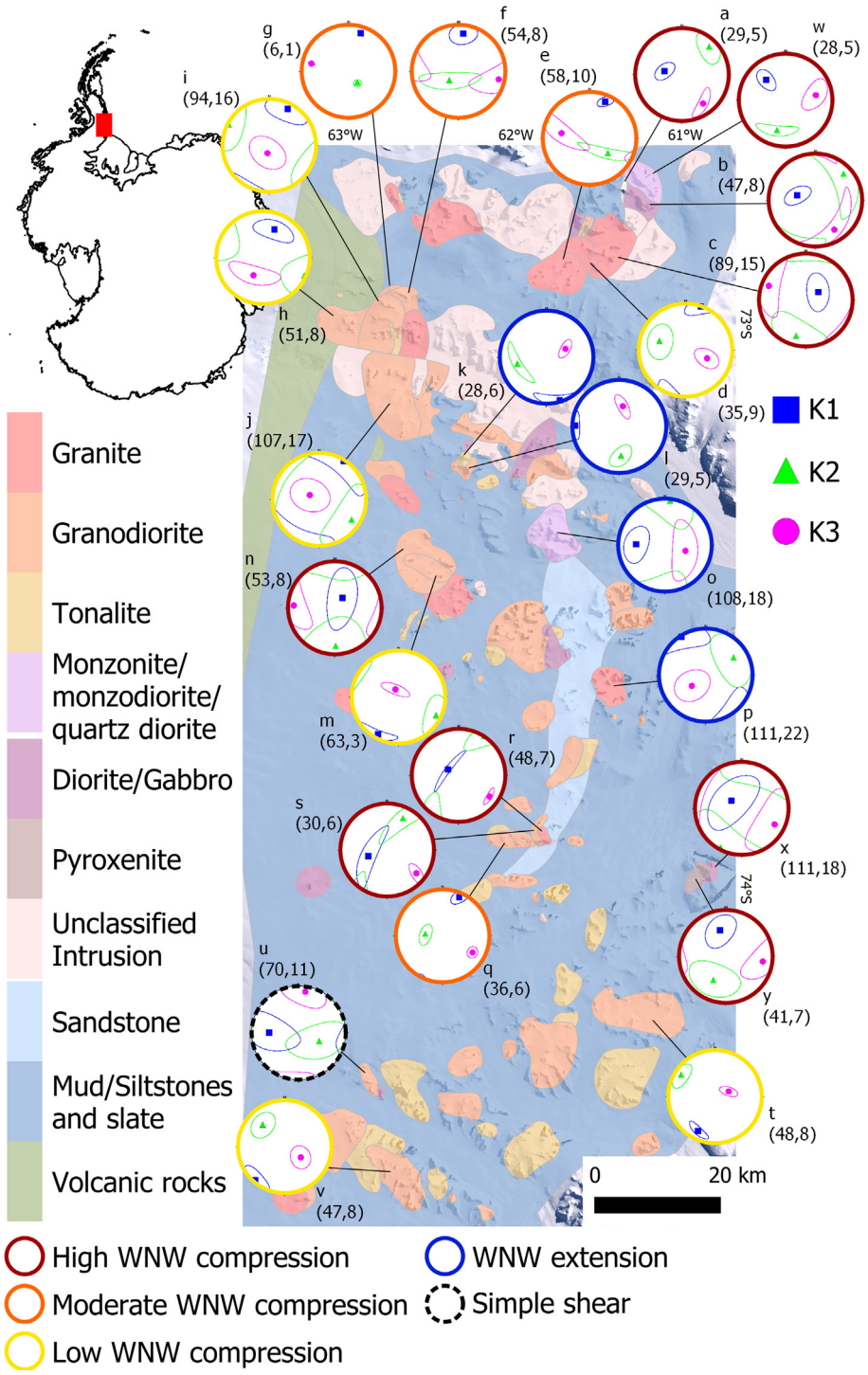

Fig. 9. Lower hemisphere stereonets of the three orthogonal axes describing the overall magnetic fabric of each analysed LCIS intrusion (K1, K2, and K3). The outline colour of each stereonet refers to the interpreted *syn*-magmatic stress regime based on the conceptual model of Fig. 3. Number of oriented cores analysed for each stereonet shown in parentheses, followed by the number of sites sampled. The oldest well-constrained subduction convergence direction of the Aluk Plate beneath the Antarctic Peninsula at this latitude (i.e. after creation of the complete plate circuit at 83 Ma) is shown for reference (McCarron and Larter, 1998). Pluton ID letters as in Fig. 4 and Fig. 5.

7.1. Sierra Nevada data compilation

7.1.1. Cathedral Peak (Fig. 11a)

The ~ 580 km^2 pink, megacrystic Cathedral Peak Granodiorite is the most extensive unit in the Tuolumne Intrusive Suite. The unit occupies much of the central batholith, and is noted for its 5 cm-wide alkali feldspar megacrysts (Bateman and Chappell, 1979). The AMS foliation is generally NW-SE striking and steeply dipping, consistent with observed field foliations (Titus et al., 2005). Lineations plunge steeply, but tend to plunge west in the west of the pluton, and eastward in the east. Žák et al. (2008) showed that visible magmatic fabrics varied across the Tuolumne Intrusive Suite, noting four distinct fabrics. However, collating their data shows that on a pluton scale the macro fabrics show the same steeply dipping, NW-SE striking foliation and steeply plunging lineation as the AMS fabric (compare Fig. 12 and Fig. 11a).

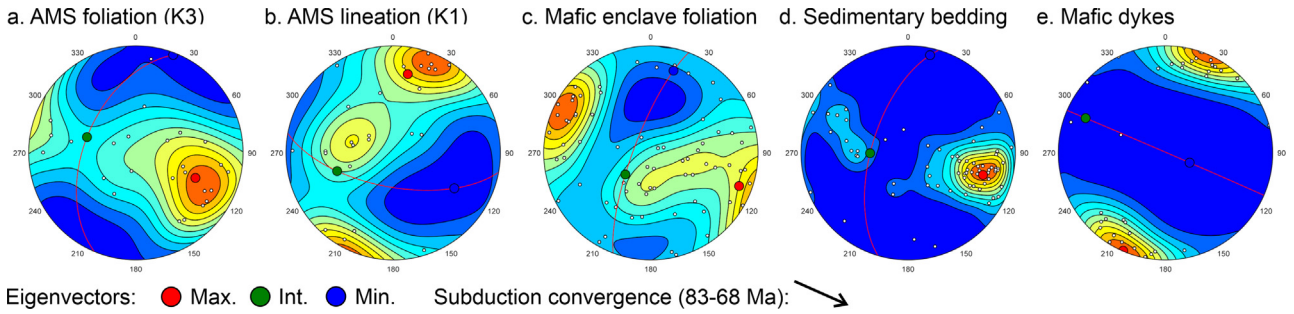

Fig. 10. 10% contours and eigenvectors for a) the poles to the AMS foliation planes of each intrusion (K3); b) the AMS lineations of each intrusion (K1); and the poles to the planes of the c) mafic enclave foliations, d) sedimentary bedding, and e) mafic dykes of the study area. All datasets record dominantly WNW-ESE oriented tectonic shortening.

7.1.2. Johnson granite porphyry (Fig. 11b)

The Johnson Granite Porphyry is the youngest and least extensive unit of the Tuolumne Intrusive Suite, located at the centre of this zoned batholith. Its variable AMS foliation poles define a NNE-SSW girdle, and its AMS lineations plunge shallowly to moderately WNW-ESE. Titus et al. (2005) interpreted the AMS fabric as magmatic as the petrography didn't show solid-state deformation, and the AMS fabric resembled the larger mineral fabrics. They used the AMS to interpret an emplacement mechanism facilitated by regional shear zones.

7.1.3. Jackass Lakes (Fig. 11c)

The Jackass Lakes Pluton is dominantly composed of medium-grained, equigranular biotite granodiorite, but is locally variable from diorite to granite. Its AMS lineation forms a NNW-SSE girdle, and its foliation dips steeply WSW-ENE. McNulty et al. (1996) interpreted this subvertical fabric as representing sheet-like assembly of the pluton.

7.1.4. Mono Creek (Fig. 11d)

The Mono Creek granite is an elongate, 55 km long pluton composed of porphyritic granite. Its overall AMS fabric has a shallowly plunging NW-SE trending lineation and a subvertical, NW-SE striking foliation. This foliation has an elongate sigmoidal form across the pluton. de Saint Blanquat and Tikoff (1997) interpreted the fabric as a magmatic fabric that was progressively rotated within a *syn*-magmatic shear zone.

7.1.5. Round Valley Peak (Fig. 11e)

The Round Valley Peak granodiorite formed slightly before and adjacent to the eastern margin of the Mono Creek granite, with magma-mixing occurring locally between the two. On a pluton scale, the AMS fabrics of this equigranular granite have a subvertical lineation and a subvertical, NW-SE striking foliation. Tikoff et al. (1999) proposed that this fabric was imparted on an incompletely-crystallised magma during forceful emplacement and lateral compression of the Mono Creek granite.

7.1.6. Silver Pass Porphyry (Fig. 11f)

The Silver Pass Porphyry is a small, late-stage intrusion within the Mono Creek granite. It has a subhorizontal, NW-SE trending AMS lineation and a subvertical, NW-SE striking foliation. Titus et al. (2005) proposed that, as for the Mono Creek granite, this fabric was imparted during emplacement along a *syn*-magmatic shear zone.

7.1.7. Shellenbarger (Fig. 11g)

The Shellenbarger granite was emplaced within the middle Cretaceous Minarets caldera. Its AMS fabric shows a subvertical AMS lineation and a subvertical, NW-SE striking foliation. Tomek et al. (2017) interpret this as a hypersolidus, coaxial tectonic deformation fabric imparted after emplacement.

7.1.8. Dinkey Creek (Fig. 11h)

The Dinkey Creek pluton is dominantly granodiorite (although ranging from granite to tonalite). Its overall AMS fabric shows a subvertical AMS lineation and a subvertical, NW-SE striking foliation, but the foliations rotate towards contact-parallel in its SW lobe, and its lineations shallow beneath the roof pendant. Cruden (1999) attributed the AMS fabric to emplacement and inflation of a tabular magma body, with shear zone deformation affecting fabrics in the pluton's eastern half.

7.1.9. Bald Mountain (Fig. 11i)

The Bald Mountain leucogranite was emplaced within the Dinkey Creek pluton ~ 7 My after the emplacement of the latter. It has a subhorizontal, NW-SE trending AMS lineation and a steep but variably dipping, NW-SE striking foliation. Tobisch and Cruden (1995) interpreted the AMS fabric as recording magma flow during emplacement via lateral spreading from NW-SE trending conduits.

7.1.10. Mt barcoft (Fig. 11j)

The AMS fabric of the dominantly granodioritic Mt Barcroft pluton is comparatively heterogeneous. Its foliation forms a girdle, with maxima indicating an overall steeply dipping NW-SE striking foliation and a shallowly to moderately plunging lineation. Michlesen (2004) attributed the fabric to heterogeneous magma flow, influenced by adjacent faults.

7.1.11. Beer creek (Fig. 11k)

The leucocratic Beer Creek granite is the youngest unit of the Eureka Valley-Joshua Flat-Beer Creek composite pluton. Its AMS fabric is comparatively heterogeneous, but has an overall steeply dipping NNW-SSE striking foliation and a subvertical lineation. Morgan et al. (2013) interpreted the fabric as representing magma flow during emplacement, imparting compressional outward deformation on the older units of the composite pluton.

7.1.12. Eureka valley (Fig. 11l)

The Eureka Valley monzonite is the smallest and oldest unit of the Eureka Valley-Joshua Flat-Beer Creek composite pluton. Its overall AMS fabric has a steeply dipping NW-SE striking foliation and a steeply plunging lineation. Morgan et al. (2013) interpreted the fabric as representing magma flow during emplacement.

7.1.13. Joshua flat (Fig. 11m)

The Joshua Flat monzonite is the intermediate unit of the Eureka Valley-Joshua Flat-Beer Creek composite pluton. Its overall AMS fabric has a steeply dipping NNW-SSE striking foliation and a steeply plunging lineation. Morgan et al. (2013) interpreted the

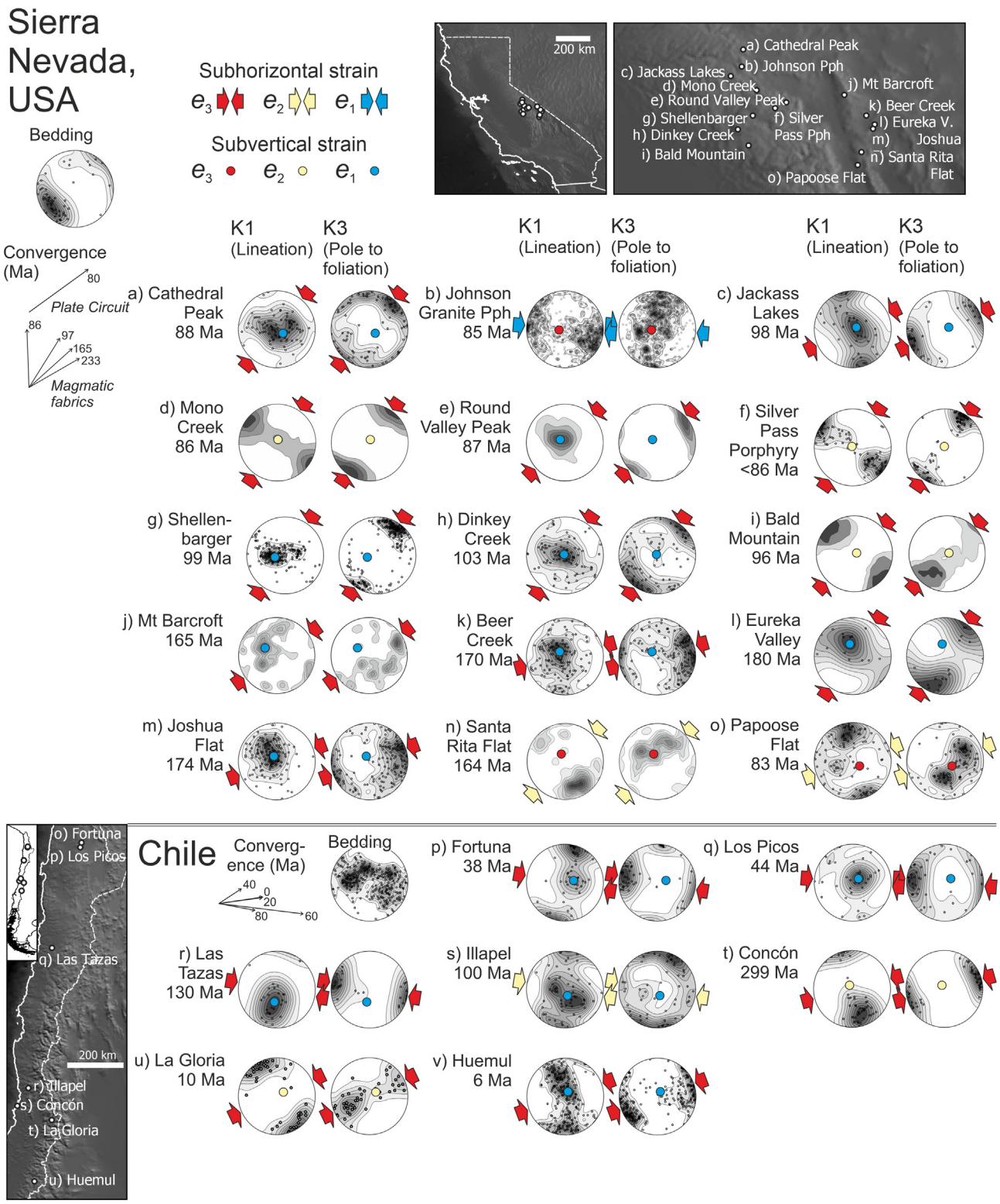

Fig. 11. Compilation of all AMS data from the plutons of the Sierra Nevada, and Chile. K1 (lineation, e_1) and K3 (pole to foliation, e_3) plotted as lower hemisphere stereonets with 10% contours and interpreted strain axes based on Fig. 1 (e_1 – Maximum extension direction; e_2 – Intermediate extension direction; e_3 – Minimum extension direction). All compiled data show dominantly tectonic, not magmatic controls. The majority display homogenous fabrics on the pluton-scale, with e_3 subparallel to the paleosubduction direction (SW-NE in California, E-W in Chile), whilst other fabrics result from variable relative magnitudes of lithostatic and tectonic compression (Fig. 13). Bedding directions from the Sierra Nevada (Cao et al., 2015) and northern Chile (Amilibia et al., 2008) are shown for comparison. Convergence directions between the relevant continental and oceanic plates are based on the global plate circuit (Wright et al., 2016) and the magmatic fabrics of the Sierra Nevada (Cao et al., 2015). A table of the AMS and geochronology data sources, number of samples analysed, and dating method used is included in the Supplementary Material.

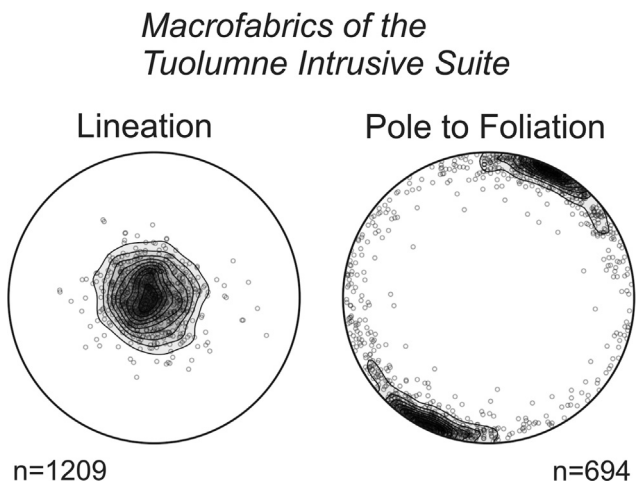

Fig. 12. Macrofabrics of the Tuolumne Batholith, combining data from Žák et al. (2008) to determine the pluton-scale fabric from local data. Compare with the similar fabrics of the Cathedral Peak AMS data in Fig. 11a.

fabric as representing magma flow during emplacement, which underwent compressional deformation during emplacement of the younger Beer Creek granite.

7.1.14. Santa rita flat (Fig. 11n)

The Santa Rita Flat granite has variable shallowly to moderately dipping foliation and a subhorizontal SSE plunging lineation. Vines and Law (2000) proposed that the variable foliation represented emplacement of the pluton as a "saddle reef" along the hinge line of a syncline during folding. However, Stevens et al. (2001) challenged this model as incompatible with the geometry and probable age of the host rock structures, with no evidence for a syncline, and that the body was more likely steep walled and continuing for considerable depth.

7.1.15. Papoose flat (Fig. 11o)

The overall AMS fabric of the granitic to granodioritic Papoose Flat pluton has a variable shallow to moderately dipping foliation and a shallowly NNW-SSE plunging lineation. The foliation defines an elongate, shallow outward dipping dome pattern, concordant with the pluton margins. de Saint-Blanquat et al. (2001) interpreted the AMS data as an emplacement fabric fed by a WNW-striking feeder dyke, with the dome shape representing inflation and lateral expansion of a laccolith.

7.2. Chile data compilation

7.2.1. Fortuna (Fig. 11p)

The granodiorite of the Fortuna plutonic complex is the younger plutonic suite of Chuquicamata in the Precordillera of northern Chile. Its AMS fabric displays a variable lineation about a NNE-SSW girdle, with a steeply plunging maxima, and its overall foliation is steeply dipping and NNE-SSW striking. Somoza et al. (2015) interpreted this fabric as representing a combination of vertical magma sheet injection and tectonic strain.

7.2.2. Los Picos (Fig. 11q)

The diorite to quartz monzonite bodies of the Los Picos plutonic complex are the older plutonic suite of Chuquicamata. Its overall AMS fabric displays a subvertical lineation, and a steeply dipping NNE-SSW striking foliation. As for the Fortuna complex, Somoza et al. (2015) interpreted this fabric as representing a combination of vertical magma sheet injection and tectonic strain.

7.2.3. Las Tazas (Fig. 11r)

The monzonitic to granodioritic Las Tazas Complex intrudes the Cordillera de la Costa of northern Chile. Its overall AMS lineation plunges steeply to moderately, and its subvertical foliation strikes NNE-SSW. Wilson (1998) explored the relationships between magnetic and macro fabrics in the complex, but did not postulate on the origin of the fabric.

7.2.4. Illapel (Fig. 11s)

The lithologically variable, Illapel Plutonic Complex (gabbro to granodiorite) was emplaced into Jurassic-Cretaceous volcanic and sedimentary sequences in central Chile. It has a heterogeneous AMS fabric, but overall maxima indicating a steeply dipping lineation and a WNW-ESE striking subvertical foliation. Ferrando et al. (2014) interpreted the AMS data as a magma emplacement fabric.

7.2.5. Concón (Fig. 11t)

The overall AMS fabrics of the Late Paleozoic granitoids of Concón in central Chile show a subhorizontal, SSE-plunging lineation and a subvertical NNW-SSE striking foliation. Creixell et al. (2006) focussed their interpretation on the Mesozoic dykes crosscutting the granitoids, and do not postulate on the origin of the granitoid fabrics.

7.2.6. La Gloria (Fig. 11u)

The quartz monzonite to granite, La Gloria pluton displays an overall AMS fabric of subhorizontal, NNW-SSE trending lineations, and a variably steep to moderately dipping NNW-SSE striking foliation. Gutierrez et al. (2013) interpreted the variable foliation as recording internal convection within the pluton.

7.2.7. Huemel (Fig. 11v)

The quartz monzonite to granite Huemel pluton of the Chilean Andes has an overall AMS fabric of a steep to moderate plunging lineation and a subvertical, NNW-SSE striking foliation. Garibaldi et al. (2018) interpreted this fabric as recording tectonic shortening, and proposed that this led to rhyolitic melt extraction.

7.3. Absent data

Whilst we attempted to include all published AMS data from the plutons of the Sierra Nevada and Chile, we recognise that some may unintentionally have been missed. Unfortunately, some studies do not include data tables or visualise the data in a manner that we could utilise (e.g. Sage Hen Flat; Morgan et al., 2000), and the data for other studies are no longer available (e.g. Mt Givens; McNulty et al., 1996). However, we are confident this data compilation accurately represents the regional AMS fabrics. We recommend further AMS publications include data tables of all analysed samples to aid future studies and maximise data utility.

7.4. Origin of East Pacific AMS fabrics

Despite the comparable pluton-scale AMS fabrics recorded by the various East Pacific studies, some authors propose a tectonic origin whilst others propose a magmatic one (e.g. compare the Shellenbarger and Dinkey Creek plutons, Fig. 11g and Fig. 11h; Cruden, 1999; Tomek et al., 2017). In the LCIS, the AMS foliation and host rock structures were all aligned relative to the *syn*-magmatic plate convergence direction of the Aluk Plate beneath the Antarctic Peninsula. This indicated a tectonic origin for the AMS fabrics. For the Californian plutons, determining relative convergence between the Pacific Ocean plates and North America is ambiguous prior to formation of a complete plate circuit at 83 Ma. Prior to 83 Ma, Pacific Plate reconstructions use mantle ref-

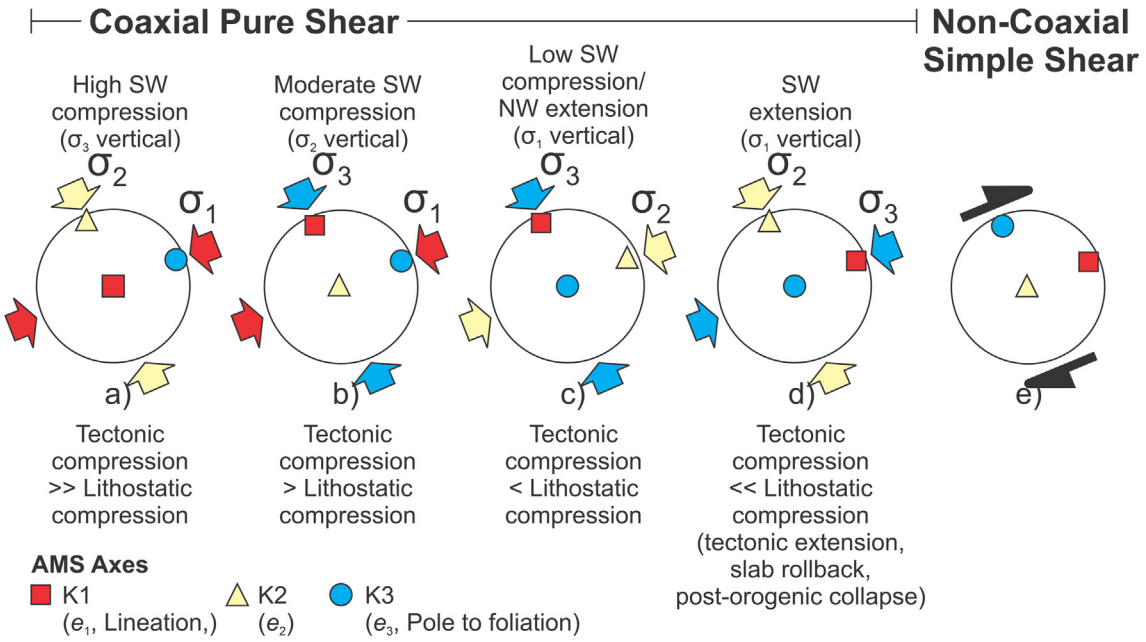

Fig. 13. Lower hemisphere stereonets for deriving the variable magnetic fabric orientations of the Sierra Nevada batholith (Fig. 11) within a regime of homogenous vertical lithostatic compression and SW-NE oriented horizontal tectonic compression of consistent orientation but variable magnitude. Shown are the principal compressive stress directions (maximum stress, σ_1; intermediate stress, σ_2; and minimum stress, σ_3), simple shear directions, and vectors of magnetic susceptibility: K1 – Maximum susceptibility and magnetic lineation; K2 – Intermediate susceptibility; K3 – Minimum susceptibility and pole to foliation. Reoriented from Fig. 3. to reflect the WSW-ENE subduction convergence direction beneath the Sierra Nevada.

erence frames instead of a plate circuit (Müller et al., 2016), despite evidence that mantle hotspots move over time (Konrad et al., 2018). It is also unclear whether any other ocean plates existed within the ~ 4600 km of now subducted ocean crust that separated the 83 Ma Pacific ocean isochrons from the continental margin (a distance and consequent uncertainty that increases farther back in time). However, orientations of bedding (322/71 NE) and host rock foliation (315/78 NE) in the Sierra Nevada (Cao et al., 2015) indicate shortening directions of approximately 52° and 45° respectively. These orientations are perpendicular to the continental margin (the continent-ocean boundary) and comparable with the ~ 50° azimuth of the Farallon Plate beneath the Sierra Nevada at 83 Ma predicted by the global plate circuit (Wright et al., 2016). Published interpretations of the convergence direction from magmatic fabric data (Cao et al., 2015) indicate similar margin-perpendicular convergence back to 232.9 Ma. However, the global plate circuit model (Wright et al., 2016) indicates continued convergence in this relative orientation in the Late Cretaceous, challenging the proposal by Cao et al. (2015) that convergence switched from normal to oblique after 90 Ma. Convergence along the Chilean margin is similarly ambiguous prior to 83 Ma, but the 80 Ma global plate circuit also indicates sub-perpendicular convergence relative to the trench since the Late Cretaceous (Wright et al., 2016). This is supported by the WNW-ESE dip of Mesozoic-Cenozoic sedimentary beds in northern Chile (Amilibia et al., 2008).

All AMS data show principal axes in these directions, in agreement with the expected stereonets associated with tectonic fabrics (Fig. 13). The majority of plutons record homogenous AMS fabrics on the pluton-scale, and high subduction-driven tectonic compression (i.e. e_3 and σ_1 are sub-perpendicular to the continental margin). Whole-pluton, East Pacific AMS fabrics thus principally record *syn*-magmatic deformation.

This ubiquitous presence of tectonic fabrics, and the homogeneity of AMS stereonets at the whole-pluton scale (Fig. 11) is despite the undeniable prevalence of visible magmatic fabrics at the outcrop scale (e.g. Paterson et al., 2019) or over localised regions of a pluton (e.g. Žák et al., 2008). Similarly, variability in AMS axes across a pluton are also widely observed (see the literature summary in Section 7.2 and 7.3). As noted earlier, this includes: internal and external contact-parallel foliations (e.g. the Mt Kinabalu pluton, Burton-Johnson et al., 2019); fabric rotation during *syn*-magmatic shearing (e.g. the sigmoidal fabric of the Mono Creek pluton [de Saint Blanquat and Tikoff, 1997], and *syn*-magmatic shearing of the Cathedral Peak Granite by the Cascade Shear Zone [Tikoff et al., 2005]); fabric rotation during emplacement of subsequent units (e.g. vertical inflation of the Papoose Flat pluton [de Saint-Blanquat et al., 2001] and lateral rotation of the Joshua Flat pluton [Morgan et al., 2013]); or mechanical interactions during crystallisation (Olivier et al., 1997). We thus cannot emphasize enough that we do not challenge the presence of these fabrics. However, on a pluton scale, both visible and magnetic mineral fabrics are largely homogenous (Bouchez, 1997; Cao et al., 2015; Olivier et al., 1997). That is, the AMS axes cluster about mean values (Olivier et al., 1997), and can be defined by the orthogonal axes of a single strain ellipse (e_1, e_2, and e_3; Fig. 1). This applies to all plutons in this compilation (Fig. 11) the prior compilation (Fig. 2), and the LCIS data (Fig. 9), and is well illustrated in Fig. 2 of de Saint Blanquat et al. (2011) where maps showing clear fabric heterogeneity across various plutons are plotted alongside stereonets showing common orientations at the pluton-scale. As local variations in AMS fabric will be incorporated in the pluton-scale data, this heterogeneity contributes to the variation of data about the common axes, but do not contribute significantly enough to diverge the overall fabric away from the tectonic and lithostatic strain axes (i.e. one axis of the strain ellipse is always subvertical, and one is always subparallel to the subduction convergence direction; Fig. 11). Consequently, even though internal heterogeneity is commonly observed, a homogenous fabric is ubiquitously observed on the pluton-sale.

Furthermore, it is worth noting that plutons do not intrude as a single body, but via incremental magma addition, rapid dyke-fed

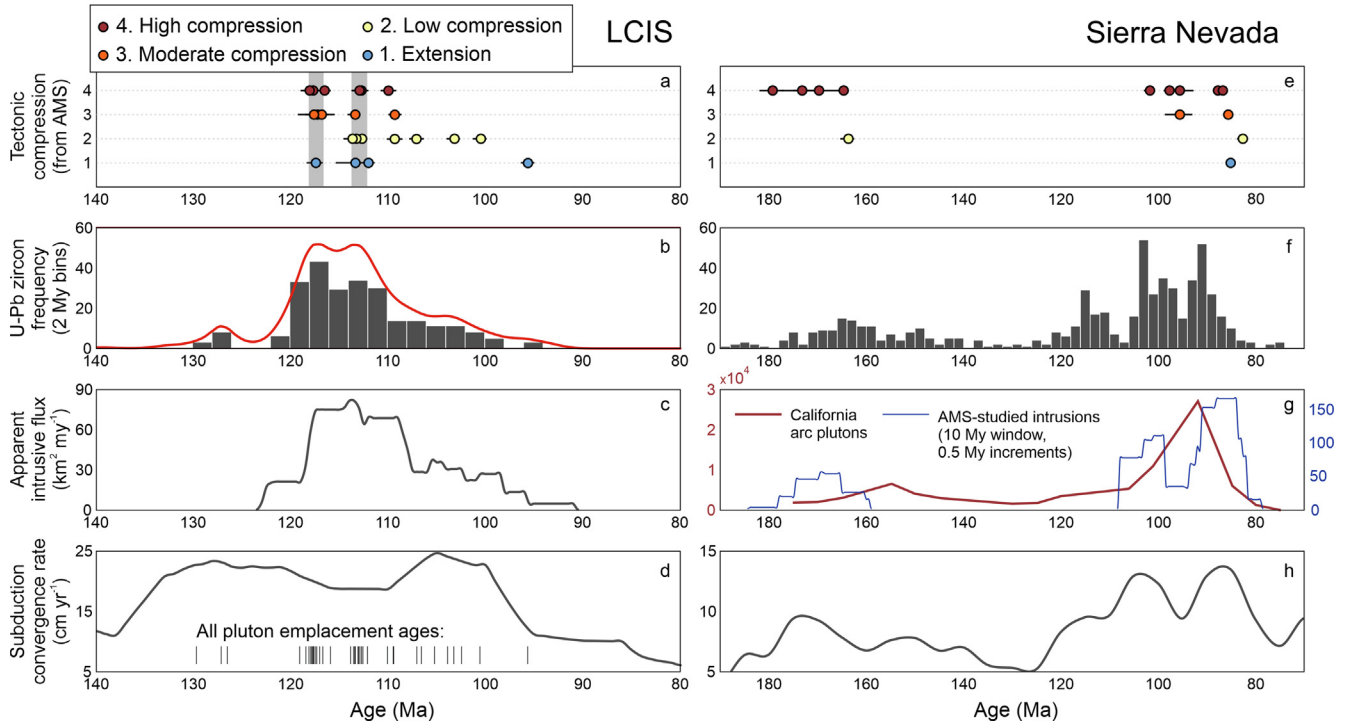

Fig. 14. The LCIS and Sierra Nevada batholith over time, showing that flare-ups are associated with high tectonic compression and end as this compression magnitude wanes. a) & e) Degree of compression against magmatic age. Data points classified by *syn*-magmatic stress regime, following Fig. 3. Grey boxes highlight the ~ 2 My composite peaks within the LCIS flare-up. b) & f) Age histogram and cumulative frequency of LCIS U-Pb zircon ages (including previous studies - (Flowerdew et al., 2005; Riley et al., 2018; Supplementary Material) and Sierra Nevada (Chapman et al., 2012). c) & g) Areal addition rates of the LCIS (based on the mapped extents of Fig. 4), the AMS-studied plutons of the Sierra Nevada (10 My intervals at 0.5 My increments), and the compilation of plutons in the California arc (65% of the arc-exposed area; Ducea, 2001). d) & h) Convergence rate between the Pacific's Aluk and Farallon Plates with the Antarctic Peninsula (Lat. 74°S, Long. 62°W) and Californian (Lat. 38°N, Long. 119°W) continental margins. Black lines in d) show individual LCIS pluton ages (including previous studies).

ascent, and layered, laccolith-style emplacement (Clemens and Mawer, 1992; Cruden, 1998; Cruden and McCaffrey, 2001; de Saint-Blanquat et al., 2006, 2001; de Silva and Gosnold, 2007; Grocott et al., 2009; Horsman et al., 2009; McCaffrey and Petford, 1997; Petford et al., 2000; Petford and Clemens, 2000; Vigneresse, 2006; Vigneresse and Clemens, 2000; Wiebe, 1988; Wiebe and Collins, 1998). Consequently, that each pluton of the East Pacific displays a homogenous AMS fabric on the pluton-scale implies that a similar strain ellipse was experienced by each subsequent batch of crystallising magma, and that the tectonically-dependant strain regime that principally determined the AMS fabric development lasted longer than the crystallisation period of each pluton.

That the data compiled from Antarctica, Chile, and the Sierra Nevada consistently display a dominance of pure shear tectonic fabrics over magmatic fabrics supports the similar conclusion of Pitcher (1997), which we quote in full: "The fabrics of what I take to represent free flowage are rarely identifiable in granitic plutons. The well organized linear fabric that we map, and often label as a magmatic foliation, is normally an indication of strain, and induced by pure shear of a progressively strengthening, viscid, crystal suspension – probably not long before the crystal framework finally linked up".

8. Tectonic control on episodic magmatism

For the LCIS, the AMS variability about common axes reveals variable *syn*-magmatic tectonic compression and crustal shortening during emplacement. U-Pb ages and mapping show most emplacement took place between 118 and 110 Ma (Fig. 14a to Fig. 14c), followed by sparse magmatism until 95 Ma. The magmatic flare up includes two composite pulses of activity (118–117 Ma, and 114–112 Ma, Fig. 14a), occurring ~ 3 My apart (outside of geochronological error; Fig. 5 and Fig. 14a). These composite pulses are consistent with the regional geochronology of Riley et al. (2018), who described three longer duration magmatic events at 130–126 Ma, 118–112 Ma and 108–102 Ma. This is reflects the fractal relationship described by de Silva et al. (2015) that within each longer duration pulse (5 to 6 Myr) will be a sequence of shorter duration (~1.5 Myr) pulses.

Integrating the U-Pb and AMS data requires within-error synchronicity. The closure temperature for Pb in zircon is 900 °C (Cherniak and Watson, 2003), whilst mineral fabrics can be developed until final locking of the crystal framework in the late stages of crystallisation, close to the solidus temperature (~690 °C for upper crustal granites; Johannes, 1984). Cooling over this interval for the centre of a 5 km wide, 2 km thick granite pluton in the Upper Crust takes ~ 52 ka (Nabelek et al., 2012). This is more than an order of magnitude less than the geochronological uncertainty on our samples, so it is reasonable to use the U-Pb ages to date the formation of AMS fabric development.

Plotting the interpreted tectonic deformation regime of the LCIS against the U-Pb ages reveals a relationship between magmatic pulses and increased tectonic compression. Moderate to high degrees of *syn*-magmatic tectonic compression are only recorded during the flare-up event, and represent the majority of the intrusions (Fig. 14a). In contrast, all of the plutons of the later waning magmatism record low levels of WNW-ESE oriented tectonic compression, and finally WNW-ESE crustal extension (Fig. 14a). Inter-

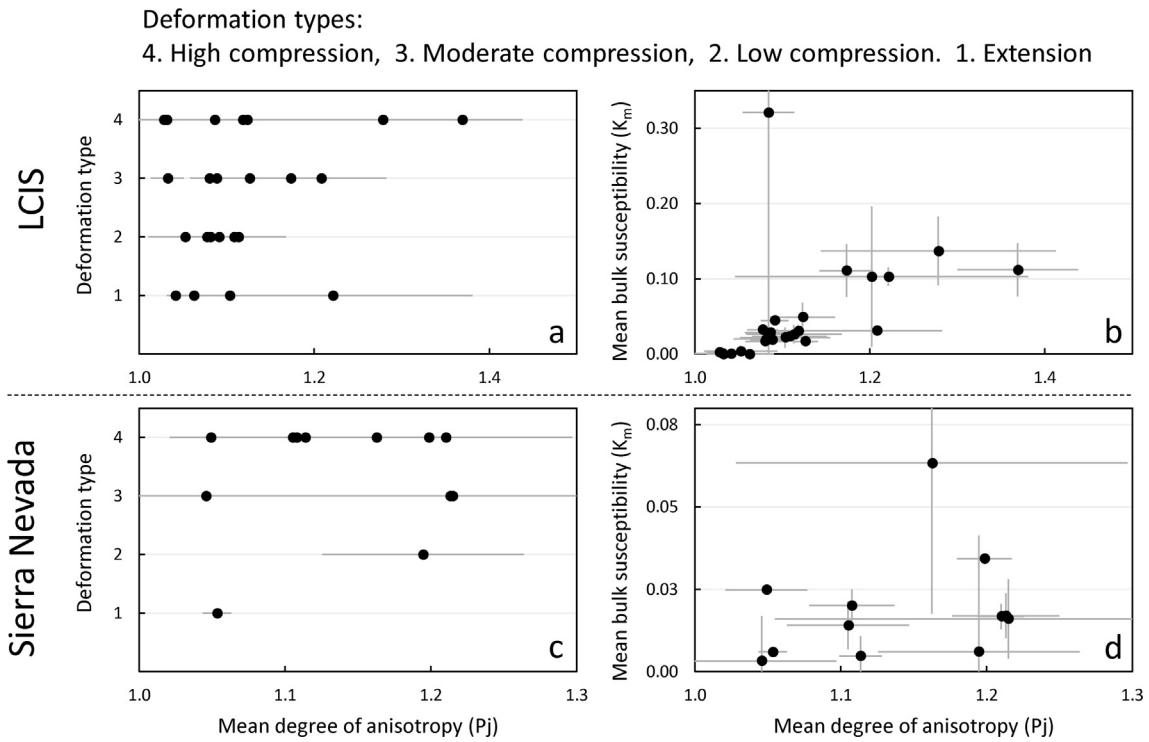

Fig. 15. Comparison of the corrected degree of anisotropy (Pj) for the LCIS and Sierra Nevada with the determined deformation type (a, c) and mean bulk susceptibility (K_m, SI units) of each pluton. ± 1 SD error bars shown.

estingly, and outside of geochronological uncertainty, the second composite pulse of the flare-up commences with low levels of WNW-ESE tectonic compression (Fig. 14a), reaches the highest levels of tectonic compression during its peak, and ends with WNW-ESE oriented crustal extension (interpreted to represent post-orogenic extension). This implies that the period of increased compression did not persist beyond the period of the composite pulse. Geochronological uncertainty prevents the exact relative timing of the apparent range in deformation regimes within each pulse to be determined. However, it is only during these composite magmatic pulses that high degrees of compression are recorded, and the range of deformation implies that increased compression occurred in discrete events.

Following the same approach applied to the LCIS, we can categorise the tectonic regimes of the Sierra Nevada using the predicted orientations of Fig. 13 (reoriented from Fig. 3 to represent the subduction convergence directions of the Sierra Nevada) and the AMS data compilation of Fig. 11. This shows emplacement during two flare-ups (180–150 Ma and 120–80 Ma, Fig. 14g). As for the LCIS, both flare-ups are during increased tectonic compression, and end with decreasing compression and crustal extension. Decreased compression midway during the younger event is contemporaneous with decreased U-Pb zircon abundance, indicating an intermediate period of reduced magmatism.

Unfortunately, the data for Chile is too sparse both temporally and geographically for a similar analysis (7 plutons over 1,550 km and 260 Ma). However, of the seven plutons, four record high-degree *syn*-magmatic compression and two record moderate compression (i.e. display a subvertical foliation plane; compare Fig. 11p to Fig. 11v with the conceptual stereonets of Fig. 13). This indicates that intrusive magmatism in Chile preferentially occurs during periods of increased tectonic compression, as previously proposed for the central and southern Andes (Horton, 2018).

AMS analytical outputs include the corrected degree of anisotropy (Pj), describing the deviation of the AMS fabric from a sphere. Given our conclusion that AMS fabrics dominantly record tectonic strain, it would be appealing if this value provided another proxy for the degree of *syn*-magmatic strain (Cogné and Perroud, 1988). However, no apparent correlation exists between Pj and the qualitative classification of deformation (Fig. 15a and Fig. 15c) for the LCIS or Sierra Nevada. A weak correlation does exist between the bulk susceptibility (K_m) and Pj (Fig. 15b and Fig. 15d), particularly for the LCIS. This indicates that a range of Pj can be developed in all settings, and that the mineralogy and associated Fe concentration has a greater effect on the degree of anisotropy than the deformation regime. This has previously been noted where the magnetic carrier phase is biotite (Biedermann, 2018; Biedermann et al., 2014) or amphibole (Biedermann et al., 2015).

It is important to reiterate here that under any suprasubduction deformation regime, the strain axes remain orthogonal: one in the vertical direction, one relative to the subduction convergence direction, and one perpendicular to these. Progressive strain is experienced by any pluton remaining ductile within these regimes, not just those in high compressional regimes, and so a range of Pj should be expected to develop in any setting. The duration of crystallisation is thus likely another parameter affecting Pj, as is the degree of strain (Cogné and Perroud, 1988), but the deformation setting is not.

This combination of U-Pb and AMS data indicates that both the LCIS and Sierra Nevada batholith were largely emplaced during flare-up events driven by tectonic deformation of the crust. Invoking a tectonic control on magmatic flare-up events is not dissimilar to previous work (De Silva et al., 2015; Kirsch et al., 2016; Matthews et al., 2012). However, Ducea (2001) found no relationship between apparent intrusive flux and the rate or obliquity of convergence, despite the expected increase in volatile flux and mantle wedge convection. Convergence rates of the Aluk Plate beneath the Antarctic Peninsula and the Farallon Plate beneath California can be calculated in GPlates (https://www.gplates.org; Boyden et al., 2011) from Matthews et al., (2016), which we have extended from 120.6 to 190 Ma using the motion of the Hikurangi–Manihiki Plateaus (Seton et al., 2012). By comparing the tim-

ing of LCIS emplacement (including Flowerdew et al., 2005, and Riley et al., 2018) with the convergence rates (Fig. 14d) we can see that whilst the LCIS plutons were emplaced within the 138–95 Ma period of increased convergence, their timing is not evenly distributed through this period. Nor does the period of maximum magmatic addition coincide with the period of maximum convergence. As shown by Ducea (2001), there is no obvious relationship between convergence rate and timing or scale of magmatism in the Sierra Nevada (Fig. 14h). However (as noted above), the absence of a complete plate circuit prior to 83 Ma renders these convergence estimates increasingly ambiguous farther back in time. These findings show that whilst flare-up events may occur within longer periods of increased subduction rates (as in the LCIS), shorter periods of enhanced tectonic compression control the timing of individual pulses.

In addition to convergence rate, the obliquity of convergence has also been proposed as a driver for flare-up magmatism (Glazner, 1991; Tikoff and de Saint Blanquat, 1997). Again, the lack of a complete plate circuit prior to 83 Ma makes calculating the angle of obliquity during these Cretaceous events even more ambiguous than the convergence rate (papers presenting such data should thus be clearer in this caveat). However, as noted above, the bedding directions of the host rocks, *syn*-magmatic dyke orientations, and plate convergence directions after 83 Ma all indicate consistent plate convergence sub-perpendicular to the plate margin. Furthermore, as noted in Equation (1) (Section 1.2), strain "refraction" occurs during oblique plate convergence. This results in the horizontal shortening direction (e_3) being closer to perpendicular with the plate margin than the relative convergence directions would imply (Teyssier et al., 1995), reducing the effects of oblique convergence.

As highlighted here, Engebretson et al. (1985) also noted that plutonism is associated with moderate to high rates of convergence, but that a high rate of convergence does not necessarily produce magmatism. The apparent lack of direct correlation between convergence rate and magmatism can be explained using the AMS data. Convergence rate at subduction zones is not expected to directly relate to compression, as supra-subduction settings in the overriding plate are frequently extensional. The global distribution of seismic events show that it is the coupling of the two plates is more important. To a first order, subduction zones of high global seismicity are characterised by high convergence rates (Ruff and Kanamori, 1980). However, along individual continental margins, seismicity is not evenly distributed, despite consistent convergence rates. Instead, seismicity (and thus interplate coupling) is spatially related to features on the seafloor or on the overriding plate (Habermann et al., 1986).

Previous studies support that interplate-coupling and resultant deformation drive magmatic flare-ups. Integrating structural, stratigraphic, and igneous records revealed a temporal and spatial relationship between tectonic and magmatic regimes along the Andes (Horton, 2018). Similar to our results, they also could not explain the timing of the magmatic and deformation events exclusively via the plate convergence history, although there was a first-order relationship with the trench-normal absolute overriding plate velocity. It was proposed that interplate coupling, driven to a first order by the rate of overriding plate advance, and to a second order by the dip of the subducting slab (increased compression and magmatism during slab shallowing) controlled the structural and magmatic history of the Andes. Horton (2018) also identified a synchronous episodicity to the Andean deformation and magmatism, which has also been identified in the Sierra Nevada based on mineral fabrics and structural data (Cao et al., 2015). This relationship is further evidenced by our data, although only the AMS data reveal the relative orientations of the principle strain axes, and the switch from high tectonic compression during the peak of each flare-up, to low tectonic compression or crustal extension terminating each flare-up.

Magmatic flare-ups of the East Pacific continental margin thus occurred during discrete events of high *syn*-magmatic tectonic compression, resulting from discrete periods of enhanced interplate coupling. Whilst high convergence rates at subduction zones may be necessary for the first order peaks in magmatism (Matthews et al., 2012) (as with seismological activity, and shown by the LCIS data and convergence model), it is these periods of increased interplate coupling and consequent increased upper plate deformation that trigger the episodic pulses of elevated magma addition rates.

9. Origin of the tectonic control on magmatism

We have shown that magmatic flare-ups are associated with increased compression, indicating that enhanced tectonic compression either increases melting in the source region or enhances melt extraction. This agrees with the breadth of evidence for the intrinsic role of deformation in the segregation, ascent, and emplacement of granitoid melts in the continental crust (Petford et al., 2000). Sr, Nd, and Pb isotopic data for East Pacific flare-up magmatism (Ardila et al., 2019) indicates a dominantly mantle source with only < 20–30 % crustal assimilation. However, partial melting of the mafic lower crust or a newly accreted mafic underplate (e.g. Petford and Gallagher, 2001) would be isotopically indistinguishable from mantle derived magmatism. We propose two hypotheses for future research, to be tested geochemically:

9.1. Hypothesis 1: Enhanced melt generation

Previous studies proposed that enhanced tectonic compression drives flare-up magmatism via crustal thickening (Cao et al., 2015), under-thrusting (Ducea, 2001), or crustal thickening and lithospheric delamination (DeCelles et al., 2009). Melting of upper and middle crustal felsic lithologies would generate crustal-affinity isotopes, not the trend towards mantle signatures observed for flare-up magmatism (Ardila et al., 2019). Consequently, melting models involving crustal thickening highlight the need to melt both mantle or lower crustal lithologies as well as incorporation of upper crustal material to generate the observed isotopic heterogeneities (DeCelles et al., 2009; Ducea, 2001). The upper crustal component can be either assimilated during magma transport or incorporated into the mantle or lower crustal source prior to melting via melange diapir ascent (Marschall and Schumacher, 2012). If thickening sufficiently increases the PT conditions to partially melt a recently accreted mafic underplate or young lower crust then this may generate felsic magmatism of indistinguishable isotopic signatures to the mantle. Once magmatism has commenced, the enhanced heat flow may decrease the bulk viscosity of the arc crust, promoting further thickening and consequent melting (Cao et al., 2015).

Whether crustal thickening can drive a magmatic flare-up revolves around the continuing debate whether continental arc magmatism is H_2O-saturated (e.g. Collins et al., 2020, 2016) or H_2O-undersaturated (e.g. Clemens et al., 2020). The H_2O-saturated model proposes that most continental margin magmatism, including the granites and calc-alkaline silicic rocks from the North American cordillera, were generated by water-fluxed partial melting of a hydrous source rather than via anhydrous dehydration melting (Collins et al., 2020, 2016). They propose that extensional, water-undersaturated adiabatic melting is more important in the backarc, although even here hydrous melting can occur (Collins et al., 2016). While anhydrous melting of ultramafic or mafic sources involves a positive PT Clapeyron slope

(Hirschmann et al., 2009; Rapp and Watson, 1995), and hence melting occurs during adiabatic decompression, the hydrous, H2O-saturated PT Clapeyron slopes are negative (Grove et al., 2012, 2006; Rapp and Watson, 1995). Consequently, in hydrous, continental margin settings, increased pressure will enhance melting of the mantle and lower crust.

9.2. Hypothesis 2: Enhanced melt segregation

Enhanced melt generation during compression is only feasible in water-saturated source regions, which may not be common systems for voluminous granitic magmatism (Clemens et al., 2020). Mantle melting is primarily a product of volatile addition, not crustal deformation (Grove et al., 2012; Schmidt and Poli, 1998), and lower crustal melting is either a product of water flux (in the hydrous melting model for batholith generation; Collins et al., 2016), basalt intrusion (Petford and Gallagher, 2001), or water-undersaturated, adiabatic decompression melting (resulting from the positive PT Clapeyron slope of mafic rocks; Rapp and Watson, 1995). Therefore, if flare-up magmatism is derived from these sources during periods of compressional deformation (Ardila et al., 2019), it can be argued that increased tectonic compression leads to enhanced melt segregation and ascent rather than increased melting of the source region. Numerical modelling shows that deformation is necessary for melt extraction from migmatites, and that pure shear compression is the most effective deformation regime; even more so than simple shear or transpression (Vigneresse and Burg, 2000). This is supported by the broad evidence associating migmatisation with contemporaneous deformation (Brown et al., 1995; Vigneresse et al., 1996).

9.3. Hypothesis 3: Enhanced melt ascent

In addition to enhancing melt segregation, enhanced compressive deformation may enhance upper crustal magmatism by aiding magma ascent. As the magmatic flare-ups cease as compression wanes, irrespective of convergence rate and associated influx of volatiles into the mantle, voluminous extraction of partial melts from the lower crust or mantle cannot be achieved when lithostatic compression is the dominant compressive stress (i.e. when σ_1 is vertical). Instead, a vertical σ_3 in response to the enhanced tectonic compression (rendering σ_1 horizontal) is required in the presence of suitable melting conditions (the orientation revealed by the AMS data to be associated with peaks in flare-up magmatism). By re-orienting the stress axes, episodes of enhanced tectonic deformation from interplate coupling thus allow voluminous mantle-derived magmas to ascend during flare-up events. Similarly, if the melts are instead derived from partial melting of a young mafic lower crust or underplate, then the partial melts require reorientation of the stress axes to escape the lower crust and reach upper crustal emplacement depths.

However, large tectonic differential stresses cannot exist in the ductile lower crust (Brown and Solar, 1998). The buoyant ascent of magma via dykes, driven by its density contrast with surrounding rocks, has been proposed by numerical models as the principal method of magma ascent through the crust (Petford, 1996). Nevertheless, magmatic overpressure (imparted by tectonic compression) may be important in the more brittle middle and upper crust, and thus control the ascent of granitic magma to its emplacement depth, including aiding space creation during emplacement (Hutton, 1997). Furthermore, increased pore-fluid pressure enables brittle behaviour at lower differential stresses, enabling brittle behaviour to extend into the lower crust through melt-enhanced embrittlement (Brown and Solar, 1998).

10. Conclusions

Although previously interpreted to record variably magmatic and tectonic fabrics, we have shown that the overall AMS fabrics of each pluton in the Antarctic Peninsula (Lassiter Coast Intrusive Suite), Sierra Nevada (California) and Chile dominantly record pure shear tectonic fabrics, imparted by strain and deformation during the final stages of their crystallisation. The AMS orientations of each pluton are dependent on the relative magnitudes of tectonic and lithostatic compression, recording the tectonic regime, and a qualitative record of the degree of *syn*-magmatic tectonic deformation.

By comparing the AMS records of the *syn*-magmatic strain axes with new and published geochronology, we have shown that increased tectonic compression during periods of enhanced interplate coupling controls intrusive magmatic flare-ups and, consequently, crustal addition in continental arcs. Whilst the Lassiter Coast flare-ups occurred during a longer period of enhanced subduction, the exact timing of the flare-up occurred during shorter periods of increased interplate coupling and resultant tectonic compression. We propose that these periods of enhanced tectonic compression triggered increased magmatic flux either by: 1) enhancing melt generation by thickening the crust, partially melting a newly accreted hydrous mafic underplate; 2) enhancing melt segregation and migmatisation in the source region; or 3) enhancing melt extraction from the mantle by rendering vertical lithostatic compression the lowest intercrustal compressive stress (σ_3) (or a combination of these processes).

CRediT authorship contribution statement

A. Burton-Johnson: Conceptualization, Methodology, Validation, Formal analysis, Investigation, Data curation, Writing – original draft, Writing – review & editing, Visualization, Project administration, Funding acquisition. **T.R. Riley:** Conceptualization, Investigation, Writing – review & editing, Project administration. **R.J. Harrison:** Resources, Writing – review & editing. **C. Mac Niocaill:** Resources, Writing – review & editing. **J.R. Muraszko:** Investigation, Visualization, Writing – review & editing. **P.D. Rowley:** Resources, Writing – review & editing.

Declaration of Competing Interest

The authors declare that they have no known competing financial interests or personal relationships that could have appeared to influence the work reported in this paper.

Acknowledgements

We thank Andrea Biedermann, Antonio Castro, Michel de St Blanquat, and an anonymous reviewer for taking the time to review and improve our manuscript, and Taras Gerya for their editorial assistance. This study is part of the British Antarctic Survey Polar Science for Planet Earth program, funded by the Natural Environmental Research Council. We wish to thank Caspar Mackeever, Dave Routeledge, Malcolm Airey, and the operations staff of the British Antarctic Survey and Rothera Base for their support. We also wish to recognise the work of the USGS geologists whose unpublished field maps and notes contributed to this research, and Hilary Blagbrough for her assistance in sample preparation. Financial support for analyses was provided by the Antarctic Science Bursary. The U-Pb zircon dating was enabled via the NERC Ion Microprobe Facility Steering Committee, and we thank them and Richard Hinton for their support.

Appendix A. Supplementary material

Supplementary data to this article can be found online at https://doi.org/10.1016/j.gr.2022.09.006.

References

Amilibia, A., Sàbat, F., McClay, K.R., Muñoz, J.A., Roca, E., Chong, G., 2008. The role of inherited tectono-sedimentary architecture in the development of the central Andean mountain belt: Insights from the Cordillera de Domeyko. J. Struct. Geol. 30, 1520–1539.

Aranguren, a., Cuevas, J., Tubıa, J.M., RomAn-Berdiel, T., Casas-Sainz, A., Casas-Ponsati, A., 2003. Granite laccolith emplacement in the Iberian arc: AMS and gravity study of the La Tojiza pluton (NW Spain). J. Geol. Soc. 160, 435–445. https://doi.org/10.1144/0016-764902-079.

Arbaret, L., Diot, H., Bouchez, J.L., Lespinasse, P., de Saint-Blanquat, M., 1997. Analogue 3D simple-shear experiments of magmatic biotite subfabrics, in: Granite: From Segregation of Melt to Emplacement Fabrics. Springer, pp. 129–143.

Ardila, A.M.M., Paterson, S.R., Memeti, V., Parada, M.A., Molina, P.G., 2019. Mantle driven cretaceous flare-ups in Cordilleran arcs. Lithos 326, 19–27.

Bateman, P.C., Chappell, B.W., 1979. Crystallization, fractionation, and solidification of the Tuolumne intrusive series, Yosemite National Park. California. Geol. Soc. Am. Bull. 90, 465–482.

Benn, K., 2010. Anisotropy of magnetic susceptibility fabrics in syntectonic plutons as tectonic strain markers: the example of the Canso pluton, Meguma Terrane, Nova Scotia. Earth Environ Sci. Trans. R. Soc. Edinb. 100, 147–158. https://doi.org/10.1017/S1755691009016028.

Benn, K., Paterson, S.R., Lund, S.P., Pignotta, G.S., Kruse, S., 2001. Magmatic fabrics in batholiths as markers of regional strains and plate kinematics: example of the Cretaceous Mt. Stuart batholith. Phys. Chem. Earth Part Solid Earth Geod. 26, 343–354. https://doi.org/10.1016/S1464-1895(01)00064-3.

Biedermann, A.R., 2018. Magnetic anisotropy in single crystals: a review. Geosciences 8, 302.

Biedermann, A.R., Bilardello, D., 2021. Practical Magnetism VII: Avoiding common misconceptions in magnetic fabric interpretation. IRM Q.

Biedermann, A.R., Koch, C.B., Lorenz, W.E., Hirt, A.M., 2014. Low-temperature magnetic anisotropy in micas and chlorite. Tectonophysics 629, 63–74.

Biedermann, A.R., Koch, C.B., Pettke, T., Hirt, A.M., 2015. Magnetic anisotropy in natural amphibole crystals. Am. Mineral. 100, 1940–1951.

Biedermann, A.R., Kunze, K., Hirt, A.M., 2018. Interpreting magnetic fabrics in amphibole-bearing rocks. Tectonophysics 722, 566–576.

Biedermann, A.R., Kunze, K., Zappone, A.S., 2020. Crystallographic preferred orientation, magnetic and seismic anisotropy in rocks from the Finero peridotite, Ivrea-Verbano Zone, Northern Italy–interplay of anisotropy contributions from different minerals. Tectonophysics 782, 228424.

Bouchez, J.L., 1997. Granite is never isotropic: an introduction to AMS studies of granitic rocks, in: Granite: From Segregation of Melt to Emplacement Fabrics. Springer, pp. 95–112.

Bouillin, J.-P., Bouchez, J.-L., Lespinasse, P., Pêcher, a., 1993. Granite emplacement in an extensional setting: an AMS study of the magmatic structures of Monte Capanne (Elba, Italy). Earth Planet. Sci. Lett. 118, 263–279. https://doi.org/10.1016/0012-821X(93)90172-6.

Boyden, J.A., Müller, R.D., Gurnis, M., Torsvik, T.H., Clark, J.A., Turner, M., Ivey-Law, H., Watson, R.J., Cannon, J.S., 2011. Next-generation plate-tectonic reconstructions using GPlates. In: Keller, G.R., Baru, C. (Eds.), Geoinformatics: Cyberinfrastructure for the Solid Earth Sciences. Cambridge University Press, pp. 95–113.

Brown, M., Averkin, Y.A., McLellan, E.L., Sawyer, E.W., 1995. Melt segregation in migmatites. J. Geophys. Res. Solid Earth 100, 15655–15679.

Brown, M., Solar, G.S., 1998. Granite ascent and emplacement during contractional deformation in convergent orogens. J. Struct. Geol. 20, 1365–1393.

Bucher, K., Grapes, R., 2011. Petrogenesis of metamorphic rocks. Springer, Heidelberg, Germany.

Burton-Johnson, A., Macpherson, C.G., Muraszko, J.R., Harrison, R.J., Jordan, T.A., 2019. Tectonic strain recorded by magnetic fabrics (AMS) in plutons, including Mt Kinabalu, Borneo: A tool to explore past tectonic regimes and syn-magmatic deformation. J. Struct. Geol. 119, 50–60. https://doi.org/10.1016/j.jsg.2018.11.014.

Burton-Johnson, A., Riley, T.R., 2015. Autochthonous v. accreted terrane development of continental margins: a revised in situ tectonic history of the Antarctic Peninsula. J. Geol. Soc. 172, 822–835.

Camp, V.E., Griffis, R.J., 1982. Character, genesis and tectonic setting of igneous rocks in the Sistan suture zone, eastern Iran. Lithos 15, 221–239.

Campbell, I.H., Ballard, J.R., Palin, J.M., Allen, C., Faunes, A., 2006. U-Pb zircon geochronology of granitic rocks from the Chuquicamata-El Abra porphyry copper belt of northern Chile: Excimer laser ablation ICP-MS analysis. Econ. Geol. 101, 1327–1344.

Cao, W., Paterson, S., Memeti, V., Mundil, R., Anderson, J.L., Schmidt, K., 2015. Tracking paleodeformation fields in the Mesozoic central Sierra Nevada arc: Implications for intra-arc cyclic deformation and arc tempos. Lithosphere 7, 296–320.

Chapman, A.D., Saleeby, J.B., Wood, D.J., Piasecki, A., Kidder, S., Ducea, M.N., Farley, K.A., 2012. Late Cretaceous gravitational collapse of the southern Sierra Nevada batholith, California. Geosphere 8, 314–341.

Chen, J.-H.-Y., 1977. Uranium-lead isotopic ages from the southern Sierra Nevada batholith and adjacent areas, California. University of California, Santa Barbara. PhD Thesis.

Cherniak, D.J., Watson, E.B., 2003. Diffusion in zircon. Rev. Mineral. Geochem. 53, 113–143.

Clemens, J.D., Mawer, C.K., 1992. Granitic magma transport by fracture propagation. Tectonophysics 204, 339–360. https://doi.org/10.1016/0040-1951(92)90316-X.

Clemens, J.D., Stevens, G., Bryan, S.E., 2020. Conditions during the formation of granitic magmas by crustal melting–hot or cold; drenched, damp or dry? Earth-Sci. Rev. 200, 102982.

Cogné, J.-P., Perroud, H., 1988. Anisotropy of magnetic susceptibility as a strain gauge in the Flamanville granite, NW France. Phys. Earth Planet. Inter. 51, 264–270.

Coleman, D.S., Briggs, S., Glazner, A.F., Northrup, C.J., 2003. Timing of plutonism and deformation in the White Mountains of eastern California. Geol. Soc. Am. Bull. 115, 48–57.

Coleman, D.S., Glazner, A.F., 1997. The Sierra Crest magmatic event: Rapid formation of juvenile crust during the Late Cretaceous in California. Int. Geol. Rev. 39, 768–787.

Collins, W.J., Huang, H.-Q., Jiang, X., 2016. Water-fluxed crustal melting produces Cordilleran batholiths. Geology 44, 143–146.

Collins, W.J., Murphy, J.B., Johnson, T.E., Huang, H.-Q., 2020. Critical role of water in the formation of continental crust. Nat. Geosci. 13, 331–338.

Cottam, M.A., Hall, R., Sperber, C., Armstrong, R., 2010. Pulsed emplacement of the Mount Kinabalu granite, northern Borneo. J. Geol. Soc. 167, 49–60. https://doi.org/10.1144/0016-76492009-028.

Creixell, C., Parada, M.Á., Roperch, P., Morata, D., Arriagada, C., de Arce, C.P., 2006. Syntectonic emplacement of the Middle Jurassic Concon mafic dike swarm, Coastal Range, central Chile (33° S). Tectonophysics 425, 101–122.

Cruden, A.R., 1999. Magnetic fabric evidence for conduit-fed emplacement of a tabular intrusion: Dinkey Creek Pluton, central Sierra Nevada batholith, California. J. Geophys. Res. Solid Earth 104, 511–530.

Cruden, A.R., 1998. On the emplacement of tabular granites. J. Geol. Soc. 155, 853–862.

Cruden, A.R., McCaffrey, K.J.W., 2001. Growth of plutons by floor subsidence: implications for rates of emplacement, intrusion spacing and melt-extraction mechanisms. Phys. Chem. Earth Part Solid Earth Geod. 26, 303–315. https://doi.org/10.1016/S1464-1895(01)00060-6.

de Saint Blanquat, M., Horsman, E., Habert, G., Morgan, S., Vanderhaeghe, O., Law, R., Tikoff, B., 2011. Multiscale magmatic cyclicity, duration of pluton construction, and the paradoxical relationship between tectonism and plutonism in continental arcs. Tectonophysics 500, 20–33.

de Saint Blanquat, M., Tikoff, B., 1997. Development of magmatic to solid-state fabrics during syntectonic emplacement of the Mono Creek Granite, Sierra Nevada Batholith, in: Granite: From Segregation of Melt to Emplacement Fabrics. Springer, pp. 231–252.

de Saint-Blanquat, M., Habert, G., Horsman, E., Morgan, S.S., Tikoff, B., Launeau, P., Gleizes, G., 2006. Mechanisms and duration of non-tectonically assisted magma emplacement in the upper crust: the Black Mesa pluton, Henry Mountains, Utah. Tectonophysics 428, 1–31.

de Saint-Blanquat, M., Law, R.D., Bouchez, J.-L., Morgan, S.S., 2001. Internal structure and emplacement of the Papoose Flat pluton: An integrated structural, petrographic, and magnetic susceptibility study. Geol. Soc. Am. Bull. 113, 976–995.

de Silva, S.L., Gosnold, W.D., 2007. Episodic construction of batholiths: insights from the spatiotemporal development of an ignimbrite flare-up. J. Volcanol. Geoth. Res. 167, 320–335.

de Silva, S.L., Kay, S.M., 2018. Turning up the heat: High-flux magmatism in the Central Andes. Elements 14, 245–250.

De Silva, S.L., Riggs, N.R., Barth, A.P., 2015. Quickening the pulse: fractal tempos in continental arc magmatism. Elements 11, 113–118.

DeCelles, P.G., Ducea, M.N., Kapp, P., Zandt, G., 2009. Cyclicity in Cordilleran orogenic systems. Nat. Geosci. 2, 251–257.

Deckart, K., Godoy, E., Bertens, A., Jerez, D., Saeed, A., 2010. Barren Miocene granitoids in the Central Andean metallogenic belt, Chile: Geochemistry and Nd-Hf and U-Pb isotope systematics. Andean Geol. 37, 1–31.

Deng, X., Wu, K., Yang, K., 2013. Emplacement and deformation of Shigujian syntectonic granite in central part of the Dabie orogen: Implications for tectonic regime transformation. Sci. China Earth Sci. 56, 980–992.

Dilles, J.H., Tomlinson, A.J., Martin, M., Blanco, N., 1997. El Abra and Fortuna Complexes: A porphyry copper batholith sinistrally displaced by the Falla Oeste. In: Actas. Presented at the 8th Congreso Geológico Chileno, pp. 1883–1887.

Ducea, M., 2001. The California arc: Thick granitic batholiths, eclogitic residues, lithospheric-scale thrusting, and magmatic flare-ups. GSA Today 11, 4–10.

Engebretson, D.C., Cox, A., Gordon, R.G., 1985. Relative motions between oceanic and continental plates in the Pacific basin.

Ernst, W.G., Coleman, D.S., Van de Ven, C.M., 2003. Petrochemistry of granitic rocks in the Mount Barcroft area—Implications for arc evolution, central White Mountains, easternmost California. Geol. Soc. Am. Bull. 115, 499–512.

Fernández-Suárez, J., Dunning, G.R., Jenner, G.A., Gutierrez-Alonso, G., 2000. Variscan collisional magmatism and deformation in NW Iberia: constraints from U-Pb geochronology of granitoids. J. Geol. Soc. 157, 565–576.

Ferrando, R., Roperch, P., Morata, D., Arriagada, C., Ruffet, G., Córdova, M.L., 2014. A paleomagnetic and magnetic fabric study of the Illapel Plutonic Complex, Coastal Range, central Chile: Implications for emplacement mechanism and regional tectonic evolution during the mid-Cretaceous. J. S. Am. Earth Sci. 50, 12–26.
Fiske, R.S., Tobisch, O.T., 1978. Paleogeographic significance of volcanic rocks of the Ritter Range pendant, central Sierra Nevada, California.
Flowerdew, M.J., Millar, I.L., Vaughan, A.P.M., Pankhurst, R.J., 2005. Age and tectonic significance of the Lassiter Coast Intrusive Suite, Eastern Ellsworth Land, Antarctic Peninsula. Antarct. Sci. 17, 443–452. https://doi.org/10.1017/S0954102005002877.
Garibaldi, N., Tikoff, B., Schaen, A.J., Singer, B.S., 2018. Interpreting granitic fabrics in terms of rhyolitic melt segregation, accumulation, and escape via tectonic filter pressing in the Huemul pluton. Chile. J. Geophys. Res. Solid Earth 123, 8548–8567.
Gillespie Jr, J.G., 1979. U-Pb and Pb-Pb ages of primary and detrital zircons from the White Mountains, eastern California, in: Geological Society of America Abstracts with Programs. p. 79.
Glazner, A.F., 1991. Plutonism, oblique subduction, and continental growth: An example from the Mesozoic of California. Geology 19, 784–786.
Golynsky, A.V., Ferraccioli, F., Hong, J.K., Golynsky, D.A., von Frese, R.R.B., Young, D. A., Blankenship, D.D., Holt, J.W., Ivanov, S.V., Kiselev, A.V., 2018. New Magnetic Anomaly Map of the Antarctic. Geophys. Res. Lett. 45, 6437–6449.
Grocott, J., Arévalo, C., Welkner, D., Cruden, A.R., 2009. Fault-assisted vertical pluton growth: Coastal Cordillera, north Chilean Andes. J. Geol. Soc. 166, 295–301.
Grove, T.L., Chatterjee, N., Parman, S.W., Médard, E., 2006. The influence of H2O on mantle wedge melting. Earth Planet. Sci. Lett. 249, 74–89.
Grove, T.L., Till, C.B., Krawczynski, M.J., 2012. The role of H2O in subduction zone magmatism. Annu. Rev. Earth Planet. Sci. 40, 413–439.
Gutierrez, F., Payacan, I., Gelman, S.E., Bachmann, O., Parada, M.A., 2013. Late-stage magma flow in a shallow felsic reservoir: Merging the anisotropy of magnetic susceptibility record with numerical simulations in La Gloria Pluton, central Chile. J. Geophys. Res. Solid Earth 118, 1984–1998.
Habermann, R.E., McCann, W.R., Perin, B., 1986. Spatial seismicity variations along convergent plate boundaries. Geophys. J. Int. 85, 43–68.
Harrison, R.J., Muraszko, J., Heslop, D., Lascu, I., Muxworthy, A.R., Roberts, A.P., 2018. An Improved Algorithm For Unmixing First-Order Reversal Curve Diagrams Using Principal Component Analysis. Geochem. Geophys. Geosystems 19, 1595–1610. https://doi.org/10.1029/2018GC007511.
Hervé, F., Munizaga, F., Parada, M.A., Brook, M., Pankhurst, R.J., Snelling, N.J., Drake, R., 1988. Granitoids of the Coast Range of central Chile: geochronology and geologic setting. J. S. Am. Earth Sci. 1, 185–194.
Hirschmann, M.M., Tenner, T., Aubaud, C., Withers, A.C., 2009. Dehydration melting of nominally anhydrous mantle: The primacy of partitioning. Phys. Earth Planet. Inter. 176, 54–68.
Horsman, E., Morgan, S., de Saint-Blanquat, M., Habert, G., Nugent, A., Hunter, R.A., Tikoff, B., 2009. Emplacement and assembly of shallow intrusions from multiple magma pulses, Henry Mountains, Utah. Earth Environ. Sci. Trans. R. Soc. Edinb. 100, 117–132.
Horton, B.K., 2018. Tectonic regimes of the central and southern Andes: Responses to variations in plate coupling during subduction. Tectonics 37, 402–429.
Hrouda, F., 1982. Magnetic anisotropy of rocks and its application in geology and geophysics. Geophys. Surv. 5, 37–82.
Hutton, D.H., 1997. Syntectonic granites and the principle of effective stress: a general solution to the space problem?, in: Granite: From Segregation of Melt to Emplacement Fabrics. Springer, pp. 189–197.
Jelínek, V., 1977. The statistical theory of measuring anisotropy of magnetic susceptibility of rocks and its application. Czech Republic, Geofyzika Brno.
Jelínek, V., Kropáček, V., 1978. Statistical processing of anisotropy of magnetic susceptibility measured on groups of specimens. Stud. Geophys. Geod. 22, 50–62.
Johannes, W., 1984. Beginning of melting in the granite system Qz-Or-Ab-An-H2O. Contrib. Miner. Petrol., 264–273
Juteau, M., Michard, A., Zimmermann, J.-L., Albarede, F., 1984. Isotopic heterogeneities in the granitic intrusion of Monte Capanne (Elba Island, Italy) and dating concepts. J. Petrol. 25, 532–545.
Kellogg, K.S., Reynolds, R.L., 1978. Paleomagnetic results from the Lassiter Coast, Antarctica, and a test for oroclinal bending of the Antarctic Peninsula. J. Geophys. Res. Solid Earth 1978–2012 (83), 2293–2299.
Kelly, N.M., Hinton, R.W., Harley, S.L., Appleby, S.K., 2008. New SIMS U-Pb zircon ages from the Langavat Belt, South Harris, NW Scotland: implications for the Lewisian terrane model. J. Geol. Soc. 165, 967–981.
Kirsch, M., Paterson, S.R., Wobbe, F., Ardila, A.M.M., Clausen, B.L., Alasino, P.H., 2016. Temporal histories of Cordilleran continental arcs: Testing models for magmatic episodicity. Am. Mineral. 101, 2133–2154.
Konrad, K., Koppers, A.A., Steinberger, B., Finlayson, V.A., Konter, J.G., Jackson, M.G., 2018. On the relative motions of long-lived Pacific mantle plumes. Nat. Commun. 9, 1–8.
Lennox, P.G., de Wall, H., Durney, D.W., 2016. Correlation between magnetic fabrics, strain and biotite microstructure with increasing mylonitisation in the pretectonic Wyangala Granite, Australia. Tectonophysics 676, 170–197.
Lennox, P.G., Forster, M.A., Williams, I.S., 2014. Emplacement and deformation ages of the Wyangala Granite, Cowra. NSW. Aust. J. Earth Sci. 61, 607–618.
Lin, W., Charles, N., Chen, Y., Chen, K., Faure, M., Wu, L., Wang, F., Li, Q., Wang, J., Wang, Q., 2013a. Late Mesozoic compressional to extensional tectonics in the Yiwulüshan massif, NE China and their bearing on the Yinshan-Yanshan orogenic belt: part II: anisotropy of magnetic susceptibility and gravity modeling. Gondwana Res. 23, 78–94.
Lin, W., Faure, M., Chen, Y., Ji, W., Wang, F., Wu, L., Charles, N., Wang, J., Wang, Q., 2013b. Late Mesozoic compressional to extensional tectonics in the Yiwulüshan massif, NE China and its bearing on the evolution of the Yinshan-Yanshan orogenic belt: Part I: Structural analyses and geochronological constraints. Gondwana Res. 23, 54–77.
Lowe, T.K., 1996. Petrogenesis of the Minarets and Merced Peak volcanic-plutonic complexes. Sierra Nevada, California.
Ludwig, K.R., 2003. User Manual for Isoplot 3.00: A Geochronological Toolkit for Microsoft Excel. Berkeley Geochronol. Cent. Spec. Publ. 4, 70.
Marschall, H.R., Schumacher, J.C., 2012. Arc magmas sourced from mélange diapirs in subduction zones. Nat. Geosci. 5, 862–867.
Martins, H.C., Sant'Ovaia, H., Abreu, J., Oliveira, M., Noronha, F., 2011. Emplacement of the Lavadores granite (NW Portugal): U/Pb and AMS results. Comptes Rendus Geosci. 343, 387–396.
Martín-Hernández, F., Hirt, A.M., 2003. The anisotropy of magnetic susceptibility in biotite, muscovite and chlorite single crystals. Tectonophysics 367, 13–28.
Matthews, K.J., Maloney, K.T., Zahirovic, S., Williams, S.E., Seton, M., Mueller, R.D., 2016. Global plate boundary evolution and kinematics since the late Paleozoic. Glob. Planet. Change 146, 226–250.
Matthews, K.J., Seton, M., Müller, R.D., 2012. A global-scale plate reorganization event at 105–100Ma. Earth Planet. Sci. Lett. 355, 283–298.
Matty, D.J., Vervoort, J., Dufrane, A., Hart, G., Student, J., Morgan, S., 2008. Growth of a Large Composite Magma System: the EJB Pluton. AGU Fall Meeting Abstracts, Eastern California., in, pp. V33A–V.
Matzel, J.E.P., Bowring, S.A., Miller, R.B., 2006. Time scales of pluton construction at differing crustal levels: Examples from the Mount Stuart and Tenpeak intrusions, North Cascades. Washington. Geol. Soc. Am. Bull. 118, 1412–1430.
McAteer, C.A., 2009. Provenance of metasedimentary sequences in the Scottish and Irish Caledonides. University College Dublin, Dublin, Ireland. PhD Thesis.
McCaffrey, K.J.W., Petford, N., 1997. Are granitic intrusions scale invariant? J. Geol. Soc. 154, 1–4. https://doi.org/10.1144/gsjgs.154.1.0001.
McCarron, J.J., Larter, R.D., 1998. Late Cretaceous to early Tertiary subduction history of the Antarctic Peninsula. J. Geol. Soc. 155, 255–268.
McNulty, B.A., Tong, W., Tobisch, O.T., 1996. Assembly of a dike-fed magma chamber: The Jackass Lakes pluton, central Sierra Nevada. California. Geol. Soc. Am. Bull. 108, 926–940.
Michlesen, K.J., 2004. Heterogeneous internal fabric of the Mount Barcroft pluton, White Mountains, of eastern California: an anisotropy of magnetic susceptibility study (PhD Thesis). Virginia Tech.
Miller, J., 1996. U/Pb crystallization age of the Papoose Flat pluton, White-Inyo Mountains, California, in: Geological Society of America Abstracts with Programs. p. A91.
Monié, P., Respaut, J.P., Brichaud, S., Bouchot, V., Faure, M., 2000. 40Ar/39Ar and U-Pb geochronology applied to Au-W-Sb metallogenesis in the Cévennes and Châtaigneraie districts (Southern Massif Central, France). Doc. BRGM Subst. Minérales Énergétiques, 77–79.
Morgan, S., Law, R., de Saint Blanquat, M., 2013. Forceful emplacement of the Eureka Valley-Joshua Flat–Beer Creek composite pluton into a structural basin in eastern California; internal structure and wall rock deformation. Tectonophysics 608, 753–773.
Morgan, S.S., Law, R.D., de Saint Blanquat, M., 2000. Papoose Flat, Eureka Valley–Joshua Flat–Beer Creek, and Sage Hen Flat plutons: Examples of rising, sinking, and cookie-cutter plutons in the central White–Inyo Range, eastern California.
Müller, R.D., Seton, M., Zahirovic, S., Williams, S.E., Matthews, K.J., Wright, N.M., Shephard, G.E., Maloney, K.T., Barnett-Moore, N., Hosseinpour, M., 2016. Ocean basin evolution and global-scale plate reorganization events since Pangea breakup. Annu. Rev. Earth Planet. Sci. 44, 107–138.
Nabelek, P.I., Hofmeister, A.M., Whittington, A.G., 2012. The influence of temperature-dependent thermal diffusivity on the conductive cooling rates of plutons and temperature-time paths in contact aureoles. Earth Planet. Sci. Lett. 317, 157–164.
Olivier, P., de Saint Blanquat, M., Gleizes, G., Leblanc, D., 1997. Homogeneity of granite fabrics at the metre and dekametre scales, in: Granite: From Segregation of Melt to Emplacement Fabrics. Springer, pp. 113–127.
Orlický, O., 1990. Detection of magnetic carriers in rocks: results of susceptibility changes in powdered rock samples induced by temperature. Phys. Earth Planet. Inter. 63, 66–70.
Otoh, S., Jwa, Y.-J., Nomura, R., Sakai, H., 1999. A preliminary AMS (anisotropy of magnetic susceptibility) study of the Namwon granite, southwest Korea. Geosci. J. 3, 31–41.
Owens, W.H., 2000. Statistical applications to second-rank tensors in magnetic fabric analysis. Geophys. J. Int. 142, 527–538.
Pankhurst, R.J., Rowley, P.D., 1991. Rb-Sr study of Cretaceous plutons from southern Antarctic Peninsula and eastern Ellsworth Land, Antarctica. In: Thomson, M.R. A., Crame, J.A., Thomson, J.W. (Eds.), Geological Evolution of Antarctica. Cambridge University Press, Cambridge, UK, pp. 387–394.
Paterson, S.R., Ardill, K., Vernon, R., Žák, J., 2019. A review of mesoscopic magmatic structures and their potential for evaluating the hypersolidus evolution of intrusive complexes. J. Struct. Geol. 125, 134–147.
Paterson, S.R., Fowler, T.K., Schmidt, K.L., Yoshinobu, A.S., Yuan, E.S., Miller, R.B., 1998. Interpreting magmatic fabric patterns in plutons. Lithos 44, 53–82. https://doi.org/10.1016/S0024-4937(98)00022-X.
Petford, N., 1996. Dykes or diapirs? Earth Environ. Sci. Trans. R. Soc. Edinb. 87, 105–114.

Petford, N., Clemens, J., 2000. Granites are not diapiric! Geol. Today 16, 180–184.
Petford, N., Cruden, A.R., McCaffrey, K.J., Vigneresse, J.L., 2000. Granite magma formation, transport and emplacement in the Earth's crust. Nature 408, 669–673. https://doi.org/10.1038/35047000.
Petford, N., Gallagher, K., 2001. Partial melting of mafic (amphibolitic) lower crust by periodic influx of basaltic magma. Earth Planet. Sci. Lett. 193, 483–499.
Petronis, M.S., O'Driscoll, B., 2013. Emplacement of the early Miocene Pinto Peak intrusion, Southwest Utah, USA. Geochem. Geophys. Geosystems 14, 5128–5145.
Petronis, M.S., O'Driscoll, B., Stevenson, C.T.E., Reavy, R.J., 2012. Controls on emplacement of the Caledonian Ross of Mull Granite, NW Scotland: Anisotropy of magnetic susceptibility and magmatic and regional structures. Geol. Soc. Am. Bull. 124, 906–927. https://doi.org/10.1130/B30362.1.
Pitcher, W.S., 1997. The nature and origin of granite, Second. Chapman & Hall, London, UK.
Rapp, R.P., Watson, E.B., 1995. Dehydration Melting of Metabasalt at 8–32 kbar: Implications for Continental Growth and Crust-Mantle Recycling. J. Petrol. 36, 891–931. https://doi.org/10.1093/petrology/36.4.891.
Riley, T.R., Burton-Johnson, A., Flowerdew, M.J., Whitehouse, M.J., 2018. Episodicity within a mid-Cretaceous magmatic flare-up in West Antarctica: U-Pb ages of the Lassiter Coast intrusive suite, Antarctic Peninsula and correlations along the Gondwana margin. Geol. Soc. Am. Bull. 130, 1177–1196.
Riley, T.R., Jordan, T.A., Leat, P.T., Curtis, M.L., Millar, I.L., 2020. Magmatism of the Weddell Sea rift system in Antarctica: Implications for the age and mechanism of rifting and early stage Gondwana breakup. Gondwana Res. 79, 185–196.
Rochette, P., Jackson, M., Aubourg, C., 1992. Rock magnetism and the interpretation of anisotropy of magnetic susceptibility. Rev. Geophys. 30, 209–226.
Rowley, P.D., 1998. Cenozoic transverse zones and igneous belts in the Great Basin, western United States: Their tectonic and economic implications. Geol. Soc. Am. Spec. Pap. 323, 195–228.
Rowley, P.D., Kellogg, K.S., Williams, P.L., Willan, C.F.H., Thomson, J.W., 1992. Southern Palmer Land and Eastern Ellsworth Land. Geological Map, 1: 500 000, BAS 500G Series, Sheet 6. British Antarctic Survey, Cambridge.
Rowley, P.D., Williams, P.L., 1982. Geology of the northern Lassiter Coast and southern Black Coast, Antarctic Peninsula, in: Craddock, C. (Ed.), Antarctic Geoscience. The University of Wisconsin Press, Madison. The University of Wisconsin Press, Madison, Wisconsin, USA, pp. 339–348.
Ruff, L., Kanamori, H., 1980. Seismicity and the subduction process. Phys. Earth Planet. Inter. 23, 240–252.
Sadeghian, M., Bouchez, J.L., Nédélec, a., Siqueira, R., Valizadeh, M.V., 2005. The granite pluton of Zahedan (SE Iran): a petrological and magnetic fabric study of a syntectonic sill emplaced in a transtensional setting. J. Asian Earth Sci. 25, 301–327. https://doi.org/10.1016/j.jseaes.2004.03.001.
Schaen, A.J., Cottle, J.M., Singer, B.S., Keller, C.B., Garibaldi, N., Schoene, B., 2017. Complementary crystal accumulation and rhyolite melt segregation in a late Miocene Andean pluton. Geology 45, 835–838.
Schmidt, M.W., Poli, S., 1998. Experimentally based water budgets for dehydrating slabs and consequences for arc magma generation. Earth Planet. Sci. Lett. 163, 361–379.
Seton, M., Müller, R.D., Zahirovic, S., Gaina, C., Torsvik, T., Shephard, G., Talsma, A., Gurnis, M., Turner, M., Maus, S., 2012. Global continental and ocean basin reconstructions since 200 Ma. Earth-Sci. Rev. 113, 212–270.
Sielfeld, G., Cembrano, J., Lara, L., 2017. Transtension driving volcano-edifice anatomy: Insights from Andean transverse-to-the-orogen tectonic domains. Quat. Int. 438, 33–49.
Somoza, R., Tomlinson, A.J., Zaffarana, C.B., Singer, S.E., Negre, C.P., Raposo, M.I.B., Dilles, J.H., 2015. Tectonic rotations and internal structure of Eocene plutons in Chuquicamata, northern Chile. Tectonophysics 654, 113–130.
Stephenson, A., Sadikun, S. t, Potter, D.K., 1986. A theoretical and experimental comparison of the anisotropies of magnetic susceptibility and remanence in rocks and minerals. Geophys. J. Int. 84, 185–200.
Stern, T.W., Bateman, P.C., Morgan, B.A., Newell, M.F., Peck, D.L., 1981. Isotopic U-Pb ages of zircon from the granitoids of the central Sierra Nevada, California. US Geol. Surv. Prof. Pap. 1185, 17 p.
Stevens, C.H., Stone, P., Miller, R.B., Andersen, D.W., Metz, J., 2001. Emplacement of the Santa Rita Flat pluton as a pluton-scale saddle reef: Comment and Reply: COMMENT. Geology 29, 1157.
Streckeisen, A., 1976. To each plutonic rock its proper name. Earth-Sci. Rev. 12, 1–33. https://doi.org/10.1016/0012-8252(76)90052-0.
Sylvester, A.G., Miller, C.F., Nelson, C.A., 1978. Monzonites of the White-Inyo Range, California, and their relation to the calc-alkalic Sierra Nevada batholith. Geol. Soc. Am. Bull. 89, 1677–1687.
Talbot, J.-Y., Chen, Y., Faure, M., 2005. A magnetic fabric study of the Aigoual-Saint Guiral–Liron granite pluton (French Massif Central) and relationships with its associated dikes. J. Geophys. Res. 110, B12106–B. https://doi.org/10.1029/2005JB003699.
Teyssier, C., Tikoff, B., Markley, M., 1995. Oblique plate motion and continental tectonics. Geology 23, 447–450.
Tikoff, B., Davis, M.R., Teyssier, C., Blanquat, M. de S., Habert, G., Morgan, S., 2005. Fabric studies within the Cascade Lake shear zone, Sierra Nevada, California. Tectonophysics 400, 209–226.
Tikoff, B., de Saint Blanquat, M., 1997. Transpressional shearing and strike-slip partitioning in the Late Cretaceous Sierra Nevada magmatic arc, California. Tectonics 16, 442–459.
Tikoff, B., de Saint Blanquat, M., Teyssier, C., 1999. Translation and the resolution of the pluton space problem. J. Struct. Geol. 21, 1109–1117.
Titus, S.J., Clark, R., Tikoff, B., 2005. Geologic and geophysical investigation of two fine-grained granites, Sierra Nevada Batholith, California: Evidence for structural controls on emplacement and volcanism. Geol. Soc. Am. Bull. 117, 1256–1271.
Tobisch, O.T., Cruden, A.R., 1995. Fracture-controlled magma conduits in an obliquely convergent continental magmatic arc. Geology 23, 941–944.
Tobisch, O.T., Renne, P.R., Saleeby, J.B., 1993. Deformation resulting from regional extension during pluton ascent and emplacement, central Sierra Nevada, California. J. Struct. Geol. 15, 609–628.
Tomek, F., Žák, J., Verner, K., Holub, F.V., Sláma, J., Paterson, S.R., Memeti, V., 2017. Mineral fabrics in high-level intrusions recording crustal strain and volcano–tectonic interactions: the Shellenbarger pluton, Sierra Nevada, California. J. Geol. Soc. 174, 193–208.
Tomlinson, A.J., Blanco, P.N., Dilles, J.H., 2010. Carta Calama, Región de Antofagasta. Servicio Nacional de Geología y Minería, Carta Geológica de Chile, Santiago, Chile.
Turek, A., Kim, C.-B., 1995. U-Pb zircon ages of Mesozoic plutons in the Damyang-Geochang area, Ryongnam massif, Korea. Geochem. J. 29, 243–258.
Vaughan, A.P.M., Eagles, G., Flowerdew, M.J., 2012a. Evidence for a two-phase Palmer Land event from crosscutting structural relationships and emplacement timing of the Lassiter Coast Intrusive Suite, Antarctic Peninsula: Implications for mid-Cretaceous Southern Ocean plate configuration. Tectonics 31, 1010.
Vaughan, A.P.M., Kelley, S.P., Storey, B.C., 2002a. Mid-Cretaceous ductile deformation on the Eastern Palmer Land Shear Zone, Antarctica, and implications for timing of Mesozoic terrane collision. Geol. Mag. 139, 465–471. https://doi.org/10.1017/S0016756802006672.
Vaughan, A.P.M., Pankhurst, R.J., Fanning, C.M., 2002b. A mid-Cretaceous age for the Palmer Land event, Antarctic Peninsula: implications for terrane accretion timing and Gondwana palaeolatitudes. J. Geol. Soc. 159, 113–116. https://doi.org/10.1144/0016-764901-090.
Vaughan, A.P.M., Storey, C., Kelley, S.P., Barry, T.L., Curtis, M.L., 2012b. Synkinematic emplacement of Lassiter Coast Intrusive Suite plutons during the Palmer Land Event: evidence for mid-Cretaceous sinistral transpression at the Beaumont Glacier in eastern Palmer Land. J. Geol. Soc. 169, 759–771.
Vigneresse, J.L., 2006. Granitic batholiths: from pervasive and continuous melting in the lower crust to discontinuous and spaced plutonism in the upper crust. Trans. R. Soc. Edinb. Earth Sci. 97, 311–324.
Vigneresse, J.L., Barbey, P., Cuney, M., 1996. Rheological transitions during partial melting and crystallization with application to felsic magma segregation and transfer. J. Petrol. 37, 1579–1600.
Vigneresse, J.L., Burg, J.P., 2000. Continuous vs. discontinuous melt segregation in migmatites: insights from a cellular automaton model. Terra Nova 12, 188–192.
Vigneresse, J.L., Clemens, J.D., 2000. Granitic magma ascent and emplacement: neither diapirism nor neutral buoyancy. Geol. Soc. Lond. Spec. Publ. 174, 1–19. https://doi.org/10.1144/GSL.SP.1999.174.01.01.
Vines, J.A., Law, R.D., 2000. Emplacement of the Santa Rita Flat pluton as a pluton-scale saddle reef. Geology 28, 1115–1118.
Walz, F., 2002. The Verwey transition - a topical review. J. Phys.: Condens. Matter 14, R285–R340.
Wiebe, R.A., 1988. Structural and magmatic evolution of a magma chamber: the Newark Island layered intrusion, Nain. Labrador. J. Petrol. 29, 383–411.
Wiebe, R.A., Collins, W.J., 1998. Depositional features and stratigraphic sections in granitic plutons: implications for the emplacement and crystallization of granitic magma. J. Struct. Geol. 20, 1273–1289.
Wiedenbeck, M., Alle, P., Corfu, F., Griffin, W.L., Meier, M., Oberli, F. v, Quadt, A. von, Roddick, J.C., Spiegel, W., 1995. Three natural zircon standards for U-Th-Pb, Lu-Hf, trace element and REE analyses. Geostand. Newsl. 19, 1–23.
Willan, R.C.R., 2003. Provenance of Triassic-Cretaceous sandstones in the Antarctic Peninsula: implications for terrane models during Gondwana breakup. J. Sediment. Res. 73, 1062–1077.
Wilson, J., 1998. Magnetic susceptibility patterns in a Cordilleran granitoid: the Las Tazas complex, northern Chile. J. Geophys. Res. Solid Earth 103, 5257–5267.
Wilson, J., Dallmeyer, R.D., Grocott, J., 2000. New 40Ar/39Ar dates from the Las Tazas complex, northern Chile: Tectonic significance. J. S. Am. Earth Sci. 13, 115–122.
Wright, N.M., Seton, M., Williams, S.E., Mueller, R.D., 2016. The Late Cretaceous to recent tectonic history of the Pacific Ocean basin. Earth-Sci. Rev. 154, 138–173.
Žák, J., Tomek, F., Svojtka, M., Vacek, F., Kachlík, V., Ackerman, L., Ježek, J., Petronis, M.S., 2021. Distributed crustal shortening followed by transpressional shearing in the Superior Province, northeastern Canada: A Late Archean analogy to modern accretionary plate margins? Precambr. Res. 362, 106322.
Žák, J., Verner, K., Týcová, P., 2008. Multiple magmatic fabrics in plutons: an overlooked tool for exploring interactions between magmatic processes and regional deformation? Geol. Mag. 145, 537–551. https://doi.org/10.1017/S0016756808004573.